OCEAN TEMPERATURES IN THE LATE ORDOVICIAN: A CLUMPED ISOTOPE STUDY OF BRACHIOPODS AND CEMENTS

A Thesis

by

BRYCE B BARNEY

Submitted to the Office of Graduate and Professional Studies of
Texas A&M University
in partial fulfillment of the requirements for the degree of

MASTER OF SCIENCE

Chair of Committee,	Ethan L. Grossman
Committee Members,	Franco Marcantonio
	Michael Pope
Head of Department,	Julie Newman

December 2020

Major Subject: Geology

ABSTRACT

Throughout the Phanerozoic, $\delta^{18}O$ of carbonate fossils displays an increasing trend of -8‰ VPDB in the Cambrian to approximately -1‰ VPDB in the modern. This trend has led to three different hypotheses: 1) sea surface temperatures decreased through the Phanerozoic; 2) $\delta^{18}O$ of seawater rose through the Phanerozoic, or 3) diagenesis has altered older samples more than younger samples. To test these hypotheses, we used clumped isotope thermometry on Late Ordovician brachiopod shells and internal cements from the Cincinnati Arch in North America.

The brachiopod shells yield Δ_{47} temperatures of 25-61°C, and $\delta^{18}O_{H2O}$ values calculated from Δ_{47} temperatures and the ^{18}O paleotemperature equation of Kim and O'Neil (1997) provide values of -2.9 to 4.8‰ VSMOW. The quasi-lognormal data distribution suggests partial reordering of some of the shells; however, interpretation of brachiopod temperature data was limited to the modal data (30-35 °C), representing the original temperature distribution. Cement Δ_{47} temperatures (17-85° C) average higher than those of brachiopod shells, as are calculated $\delta^{18}O_{H2O}$ values (-5.7 to 4.4‰ VSMOW). Calculated $\delta^{18}O_{H2O}$ of the brachiopods echo previous studies suggesting that seawater $\delta^{18}O$ has not changed more than ± 1‰ throughout the Phanerozoic and that the trend seen in the $\delta^{18}O$ of carbonate fossils is a product of higher temperatures during the early Paleozoic with cooling towards the modern.

Clumped isotope analyses of cements, aided by cathodoluminescence microscopy, can provide the progression from sea surface to shallow burial to deep

burial temperatures. Cements show uniform cathodoluminescence and $\delta^{18}O$ values mostly similar to those of the best-preserved brachiopod fossils indicating that these cements formed in a marine setting. Based on the burial history of the units, the brachiopods and cements did not reach the threshold of 100 °C necessary to begin reordering clumped carbonate bonds. However, the higher Δ_{47} temperatures and $\delta^{18}O_{H2O}$ values and similar $\delta^{18}O_{carb}$ values of cements compared with brachiopods indicate greater solid-state reordering in the cements. The brachiopod shell results support the contention of warm early Paleozoic oceans while the cement results imply that the chemistry of different calcitic materials such as calcites rich in Mn, can have different reordering rates.

DEDICATION

To my loving and patient wife, Denise.

ACKNOWLEDGEMENTS

I would like to thank my committee chair, Dr. Ethan Grossman, and my committee members, Dr. Franco Marcantonio and Dr. Michael Pope, for their guidance and support throughout this research. I would like to Dr. Luz Romero for her help with the trace element analyses and Dr. Chris Maupin and Zeyang Sun for their help in maintaining and running the clumped carbonate isotope instrument. Thanks to the Cincinnati Natural History Museum & Science for allowing access to their fossil collections. Also, thanks to Dr. Brenda Hunda from the Cincinnati Museum of Natural History & Science and Don Bissett from the Cincinnati Dry Dredgers for their help with fossil collection in the field.

CONTRIBUTORS AND FUNDING SOURCES

Contributors

This work was supervised by a thesis committee consisting of Professors Ethan L. Grossman (advisor), and Michael Pope of the Department of Geology and Geophysics, and Professor Franco Marcantonio of Department of Oceanography.

The trace element analyses were performed by Dr. Luz Romero at Texas A&M University.

All other work conducted for the thesis was completed by the student independently.

Funding Sources

This graduate study was supported a graduate teaching assistantship from Texas A&M University, and the Travis Parker & Robert Berg Graduate Geology Fellowship. It was also sponsored by the Michel T. Halbouty Chair in Geology.

TABLE OF CONTENTS

Page

LIST OF FIGURES

Page

LIST OF TABLES

Page

1. INTRODUCTION

The study of paleoclimate advanced significantly with the discovery of oxygen isotope thermometry (Epstein et al., 1953). Oxygen isotope measurements reveal an intriguing trend through the rock record. Throughout the Phanerozoic, oxygen isotopic values for carbonate fossils display an increasing secular trend of -7 to -8‰ VPDB in the Cambrian to near -1‰VPDB in the modern (figure 1) (Grossman, 2012b; Qing and Veizer, 1994; Rasmussen et al., 2016; Shields et al., 2003; Veizer and Prokoph, 2015; Wadleigh and Veizer, 1992).

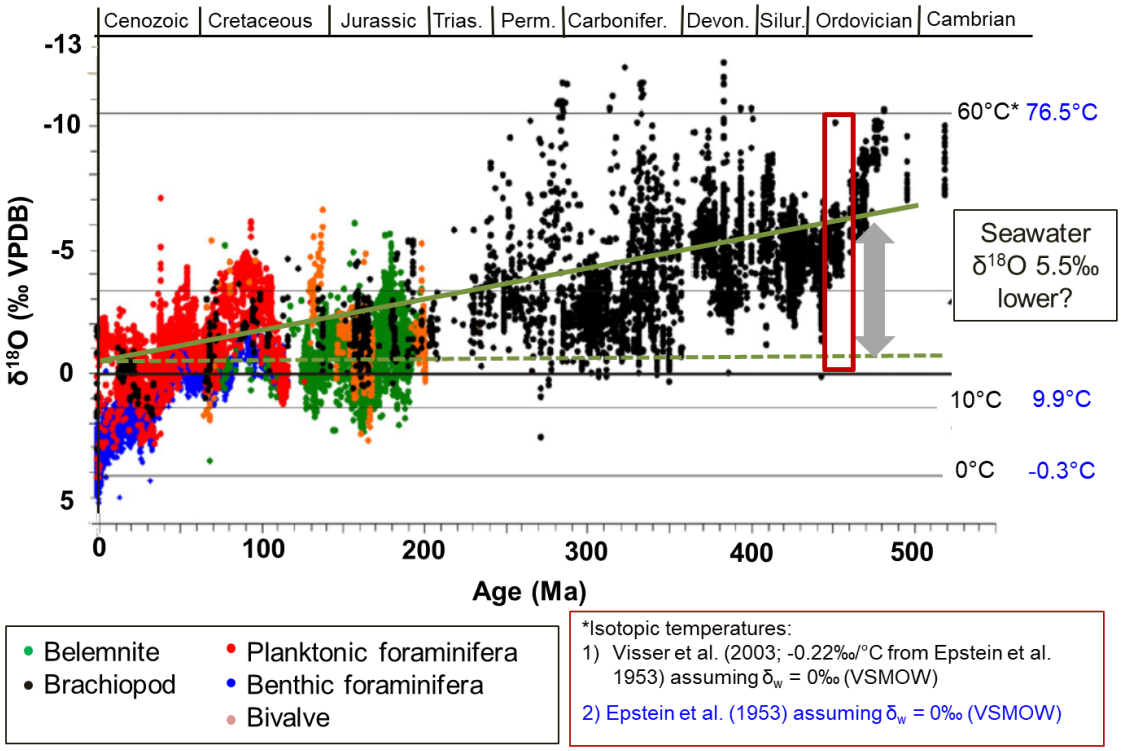

Figure 1. Secular trend of $\delta^{18}O$ during Phanerozoic low-Mg calcitic macro- and microfossils. Red box indicates the studied interval. Adapted from Veizer and Prokoph (2015).

This secular trend has been interpreted differently by different authors and has led to three hypotheses: 1) sea surface temperatures have decreased through the Phanerozoic, 2) the oxygen isotopic composition of seawater has risen through the Phanerozoic or 3) diagenesis has altered older samples more than younger samples. Several authors contend that the oxygen isotopic composition of seawater is buffered by seawater/rock interactions at the mid-ocean ridges and by continental weathering. This buffering allows for the isotopic composition of seawater to remain somewhat stable throughout deep time, causing changes in mean sea surface temperatures (MSST) to be the source of this variation (Bergmann et al., 2018; Came et al., 2007; Coogan et al., 2019; Finnegan et al., 2011; Henkes et al., 2018; Hodel et al., 2018; Muehlenbachs, 1998;). Other authors maintain the secular trend is the result of Earth processes changing the oxygen isotopic composition of seawater, such as changes in the high-temperature seawater/rock interactions at mid-ocean ridges, while the long-term (100-myr) MSST has remained relatively constant throughout the Phanerozoic (Jaffrés et al., 2007; Veizer et al., 1999; Veizer and Prokoph, 2015; Wallmann, 2001). Meteoric diagenesis can lower the $\delta^{18}O$ values of marine fossils through time (Degens and Epstein, 1962; Joachimski et al., 2004, 2009). Meteoric diagenesis is a likely explanation for some low and variable $\delta^{18}O$ values in isotopic studies. However, using techniques such as cathodoluminescence petrography (Popp et al., 1986) and microsampling to target well-preserved parts of the shell, the original isotopic signal can be determined.

The nature of oxygen isotope thermometry causes this uncertainty in interpretation. The oxygen isotope thermometer is dependent on two unknown variables,

the $\delta^{18}O$ of the ambient seawater and the precipitation temperature. Epstein et al. (1953) defined the oxygen isotope thermometer for calcite as:

$$T(°C) = 16.5 - 4.3(\delta^{18}O_{CaCO3} - \delta^{18}O_{H20}) + 0.14(\delta^{18}O_{CaCO3} - \delta^{18}O_{H20})^2 \quad (1)$$

where T is the precipitation temperature in degrees Celsius, $\delta^{18}O_{CaCO3}$ is the oxygen isotopic composition of calcium carbonate relative to PDB, and $\delta^{18}O_{H20}$ is the oxygen isotopic composition of the formation water (see Grossman, 2012a, for discussion). The isotopic composition and temperature of the formation waters control the oxygen isotopic composition of the carbonate ions in precipitated materials (Grossman, 2012b; Hays and Grossman, 1991). Thus, assumptions must be made regarding $\delta^{18}O_{H2O}$ to determine oxygen isotope paleotemperatures. Another approach must be used to acquire paleotemperatures without making assumptions about the initial precipitation conditions.

The recent development of the clumped carbonate isotope thermometer allows for the acquisition of temperatures from carbonate materials, but with one important distinction from the oxygen isotope thermometer: $\delta^{18}O_{H2O}$ need not be known (Eiler, 2007, 2011; Ghosh et al., 2006). Whereas oxygen isotope thermometer examines the heterogenous isotope exchange reaction:

$$CaC^{16}O_3 + H_2{}^{18}O = CaC^{18}O^{16}O_2 + H_2{}^{16}O \quad (2)$$

the clumped carbonate isotope thermometer examines the homogeneous isotope exchange reaction:

$$Ca^{13}C^{16}O_3 + Ca^{12}C^{18}O^{16}O_2 = Ca^{13}C^{18}O^{16}O_2 + Ca^{12}C^{16}O_3 \quad (3)$$

Equation 3 is dependent solely upon precipitation temperature, whereas equation 2 is dependent on precipitation temperature and oxygen isotopic composition of formation

waters, as previously stated. This difference allows paleotemperatures to be calculated without determining the $\delta^{18}O$ of formation waters, as must be done with conventional oxygen isotope thermometry (Eiler, 2007, 2011; Ghosh et al., 2006).

This study examines clumped carbonate isotopic measurements for Late Ordovician (Cincinnatian) brachiopods and calcitic cements from the Jessamine Dome of the Cincinnati Arch to determine subtropical sea surface temperatures during the Cincinnatian. These data help constrain the Late Ordovician paleotemperatures and ocean conditions in the epicontinental sea of Laurentia. The nature of clumped carbonate isotope thermometry allows one to determine the driving mechanism of the Phanerozoic $\delta^{18}O$ trend due to clumped carbonate isotope thermometry's sole dependence on temperature. This allows for the determination to the $\delta^{18}O$ of seawater using a calcite-H_2O fractionation relationship (e.g., Kim and O'Neil, 1997).

The Late Ordovician is a time of great interest for paleoclimatologists as it records dramatic climatic change, from warm seas at the subtropics at the start of the Katian ending with the Hirnantian glaciation (Bergmann et al., 2018; Buggisch et al., 2010; Shields et al., 2003; Tobin and Walker, 1997). The rate of cooling and the duration of this glaciation is debated. Gondwanan glacial deposits, evidence of global sea-level fall, and parallel positive carbon and oxygen isotope excursion indicate a short-term, rapid glaciation confined to the Hirnantian (Bergström et al., 2010; Brenchley et al., 1994, 2003). However, other studies suggest more long-term climate change occurring during or before the Katian starting 10 myr or more before the Hirnantian. Evidence includes 1) multiple positive carbon isotope excursions, one starting near the base of the

Katian and two more occurring within the Katian stage, 2) reports of Katian glacial deposits and 3) amplitude of shallowing upward sea level cycles (Bergström et al., 2010; Frakes et al., 2005; Pope and Read, 1997).

Studies of oxygen isotopes in fossil brachiopod shells show $\delta^{18}O$ values increasing from -6.5 to ~ -4 ‰ (figure 1) starting early in the Katian and continuing to the Hirnantian, suggesting progressive, long-term cooling instead of a short, fast cooling event (Marshall and Middleton, 1990; Qing and Veizer, 1994; Shields et al., 2003; Veizer and Prokoph, 2015; Wadleigh and Veizer, 1992). Studies of oxygen isotope values from conodonts show mixed results. Several conodont studies support cooling in the Early to Middle Ordovician but indicate a relatively stable climate through most of the Late Ordovician (Herrmann et al., 2010; Quinton and MacLeod, 2014; Quinton et al., 2018; Trotter et al., 2008). Higher resolution studies suggest an additional cooling pulse in the early Katian, and variable $\delta^{18}O$ values in conodonts across 2-6 m thick Katian-aged limestone/shale cycles with conodonts from limestone beds exhibiting high $\delta^{18}O$ values and conodonts from shale beds exhibiting lower, more variable $\delta^{18}O$ values. The authors interpreted these patterns as an effect of the waxing and waning of continental glaciers on Milankovitch times scales during the Early Katian (Buggisch et al., 2010; Elrick et al., 2013). Overall, $\delta^{18}O$ patterns in Late Ordovician conodonts are not well understood, and existing data are somewhat contradictory.

Previous clumped carbonate isotope studies (Bergmann et al., 2018; Finnegan et al., 2011) report warm sea surface temperatures (34-38 °C) early in the Katian, with the minor low-latitude cooling (~2 °C) occurring throughout the mid-Late Katian, and

dramatic low-latitude cooling (6-8 °C) occurring at the end of the Katian and into the Hirnantian. Each cooling event can be related to a positive carbon isotope excursion, with non-positive carbon isotope excursion intervals showing higher temperatures slightly above those in the modern Western Pacific Warm Pool (Bergmann et al., 2018; Finnegan et al., 2011). Trends in the $\delta^{18}O_{water}$ values calculated using clumped isotope temperatures and fossil $\delta^{18}O$ values suggest multiple episodes of moderate glaciation and melting throughout the mid-late Katian. These trends suggest that initial glaciation began in the mid-late Katian with minimal cooling in the tropics until the Hirnantian. This implies that changes in $\delta^{18}O_{carb}$ values during the Hirnantian were caused by changing temperatures, not by changes in ice volume (Finnegan et al., 2011).

This study presents conventional and clumped carbonate isotopic compositions for Late Ordovician (Cincinnatian) brachiopod shells, and the calcitic cements found within these brachiopod shells from the Jessamine Dome of the Cincinnati Arch to reconstruct the sea surface temperatures and seawater $\delta^{18}O$ during the Cincinnatian. These data help constrain the Late Ordovician paleotemperatures and ocean conditions in the epicontinental sea of Laurentia. Also, the burial history of the fossils has been better constrained using the clumped carbonate temperatures and the calculated $\delta^{18}O$ of formation waters of the cements within the interior of the brachiopod shells.

Previous clumped carbonate studies of Ordovician materials used large sample sizes, 20-60 mg (9 to 12 mg per replicate), to produce sufficient signal for the clumped carbonate measurements. These large sizes can lead to the mixing of pristine and altered materials when sampling acquire the required amount of material for the analyses. The

mixing of these different materials causes non-linear mixing effects in the clumped carbonate isotopic signal which are difficult to disentangle without knowledge of the end-member signals of the individual materials (Defliese and Lohmann, 2015). Also, these large sample sizes prevent accurate measurements of materials that occur in naturally small quantities such as individual foraminifera, and individual generations of calcitic cements.

This study uses the procedure described in Schmid and Bernasconi, (2010), which requires ten replicates of ~115 μg (1 to 1.5 mg per sample). This allows the use of microsampling techniques to limit sample material to the best-preserved shell material, and allows the measurement of individual generations of internal calcitic cements. These internal calcitic cements can be used in an effort to constrain early cementation temperatures which 1) may represent shallow groundwater and average annual temperatures for coastal environments and 2) provide minimum burial temperatures.

2. GEOLOGICAL SETTING AND SAMPLES

2.1. Geological setting

2.1.1. Paleogeography

Paleogeographic reconstructions place the Cincinnati Arch of North America in the southern subtropics, approximately 23-27°S during the first half of the Cincinnatian stage (figure 2)(Brett et al., 2012; Scotese, 2016). At the time of deposition, an epicontinental sea covered a large portion of Laurentia. Subduction and the Taconic Orogeny along eastern Laurentia created the Appalachian foreland basin, and the Cincinnati Arch was a peripheral bulge within this foreland basin. The major structural components of this arch (figure 3B) were the Nashville and Jessamine domes on the crest, the Rome trough to the south, and the Sebree trough to the north (Ettensohn et al., 2004; Kolata et al., 2001; Pope and Read, 1998; Pope et al., 2012).

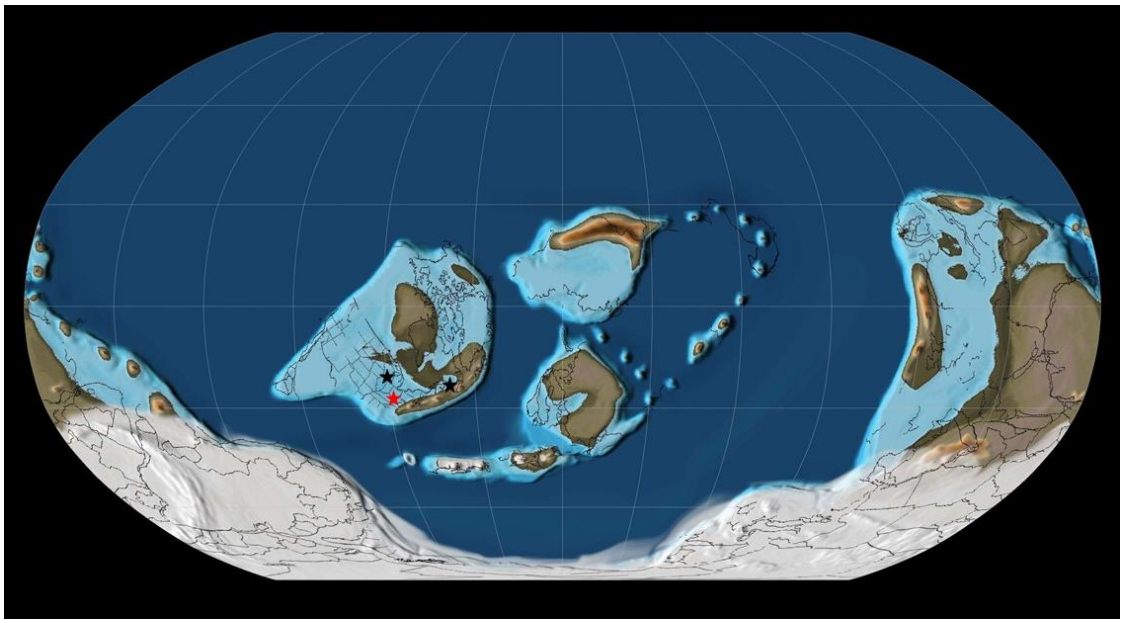

Figure 2. Paleogeographic reconstruction of the Late Ordovician period (450 Ma). Red star indicates the study area of this study, and the black stars indicate the studied areas from previous studies (Bergmann et al. (2018); Finnegan et al. (2011)). Adapted from Scotese,(2016).

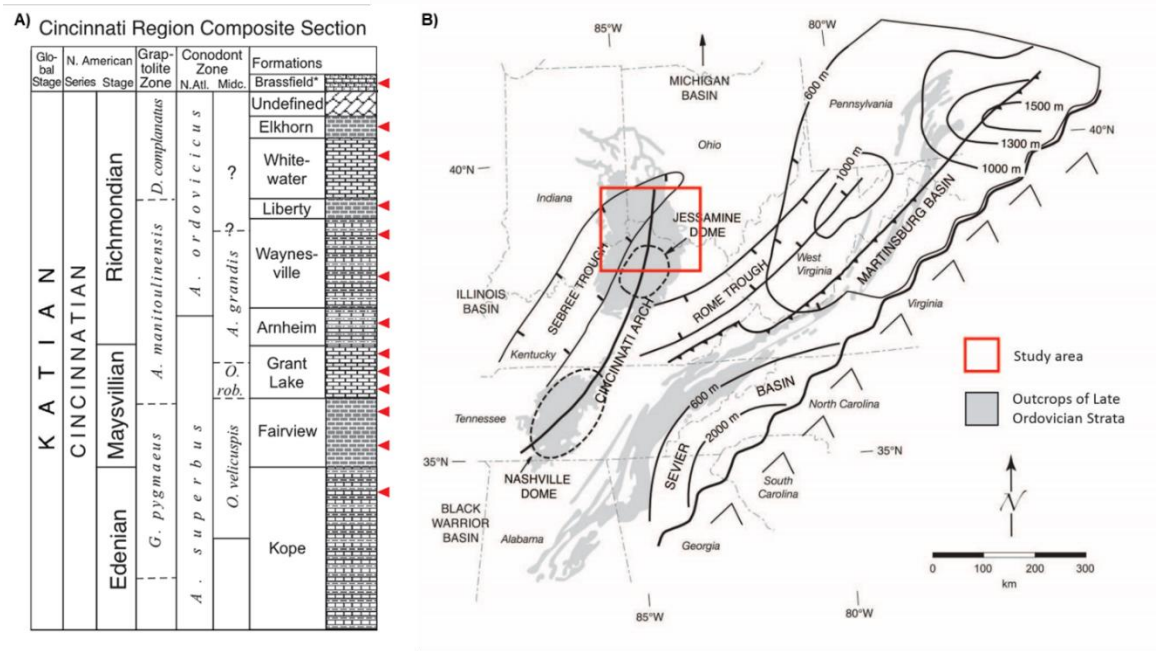

Figure 3. A) Composite Stratigraphic column of the Cincinnatian Series and underlying upper Mohawkian strata in the Cincinnati region. Red triangles indicate sampling localities. Adapted from Bergström et al., (2010). B) Map of the Cincinnati Arch and surrounding region showing study area in red, outcrop belts of Upper Ordovician rocks in gray and the principal structural features in the region. Contours indicate the thickness of Upper Ordovician sediment in the Martinsburg and Sevier basins. Adapted from Pope et al., (2012).

2.1.2. Stratigraphy

Cincinnatian strata within the study area deposited along the crest of the Jessamine Dome contain cool, temperate water, subtidal, and peritidal carbonates (figure 3A). The interbedded carbonate and shale of the Sebree and Rome troughs surround the carbonate strata on the dome (Aucoin and Brett, 2015; Brett et al., 2012; Kolata et al., 2001; Patzkowsky and Holland, 1993; Pope and Read, 1997, 1998; Pope et al., 2012).

2.1.3. Burial History

Studies of the burial history of this area suggest that these units were buried to the beginning of the oil window (~60 °C) sometime during the Late Paleozoic. Conodonts with a conodont color alteration index (CAI) of 1 are readily found within the Cincinnatian strata indicating minimal burial (<1 to 2 km), with maximum burial temperatures of < 50 to 80 °C for the Upper Ordovician sediments during the Mississippian to the early Permian(Epstein et al., 1977; Harris et al., 1978; Ryder, 1987). Burial depths were calculated using a 25 °C/km geothermal gradient with Mississippian surface Δ_{47} temperatures of 24 °C (Henkes et al., 2018).

Limited post-depositional heating (<100 °C) suggested by these studies makes fossils from this area ideal for clumped carbonate paleothermometry. Reordering of the carbonate isotopologues within the fossils should be minimal because of the moderate burial temperatures, although impossible due to exposure to the moderate burial temperatures for possibly 100 Ma or more (Hemingway and Henkes, 2020; Henkes et al., 2014; Stolper and Eiler, 2015; Stolper et al., 2018).

2.2. Samples

2.2.1. Brachiopod shells

Samples were collected from the Upper Ordovician (Cincinnatian) strata of the Jessamine Dome of the Cincinnati Arch near Cincinnati, OH. Samples were collected from Kope, Fairview, Grant Lake, Arnheim, Waynesville, Liberty, Whitewater, and Drakes formations (figure 3A). The Drakes Formation of Kentucky has been correlated to the Elkhorn Formation of Ohio and Indiana. Samples were collected in the field from shale and fossiliferous limestone beds whose locations were recorded using a handheld Garmin eTrex 20 GPS device. Specimens also were obtained from the collections of the Cincinnati Museum of Natural History & Science (Cincinnati, Ohio) and Dr. Seth Finnegan at the University of California - Berkeley. Samples collected include 28 brachiopods of two different genera, *Vinlandostrophia* (formerly known as *Platystrophia*), and *Hebertella*. Many of these specimens contain calcite cements that were also sampled to constrain early marine diagenetic and burial temperatures.

3. METHODS

3.1. Sample Preparation

Shells were visually examined in the field and at the museum collections for evidence of alteration. Specimens showing signs of alteration, e.g., pitting, large fractures, pyritization, or weathering were not collected to be sampled. The screened samples were cleaned with deionized water and a soft brush to remove loose material. The cleaned samples were dried at 60° C for at least 48 hours and then embedded in Struers Epofix epoxy. The epoxy cured for at least 48 hours, then the samples were cut longitudinally from the front of the valve to the beak. One half of the cut sample was polished using 600 grit and then mounted onto a frosted petrographic slide using Struers Epofix epoxy. The epoxy was cured for at least 48 hours, and the excess material was cut off. The thin sections were polished using increasingly fine polishing compounds to a 3.0 µm deagglomerated alpha alumina compound.

3.2. Diagenetic Evaluation

To further screen for diagenetic alteration, a thin section of each sample was examined under standard optical microscopy for breaks in the original crystal fabric, such as filled fractures, corrosion, and secondary mineral phases (e.g., pyrite). Secondly, thin sections were viewed using cathodoluminescence (CL) microscopy with a Technosyn 8200 MKII cold cathode luminoscope. Samples were exposed to a beam current and voltage of 200-300 nA, and 10-15 kV, respectively, for 60 seconds (Flake,

2011). The presence of Mn^{2+} in the crystal lattice of calcite causes orange luminescence (figure 4), which typically indicates diagenesis in brachiopod shells (Grossman et al., 1996; Popp et al., 1986). This is because Mn^{2+} is uncommon in oxygenated bottom waters, but very common in anoxic ground and pore waters. Thus, unaltered areas of the shells should consist of non-luminescent areas free of visible dissolution and cementation features. Using a gradational scale of cathodoluminescence, the shells were labeled as non-luminescent (NL), slightly luminescent (SL), cathodoluminescent (CL), or some combination. The five categories are NL, NL/SL, SL, SL/CL, and CL (Grossman, 2012a, See figure 6). Shells were sampled from several NL shell areas, or NL/SL areas when NL areas were not available.

As a supplement to the textural examination, trace elements were used as a secondary criterion of alteration within the brachiopod shells. Diagenetic alteration can lead to an increase in Fe^{2+} and Mn^{2+}, and a decrease in Sr^{2+}. These trends are often associated with depletions in $\delta^{13}C$ and $\delta^{18}O$ (Brand and Veizer, 1980; Brand et al., 2012). For these trace element analyses (Ca, Fe, Mg, Mn, Na, and Sr), aliquots of ~110 μg of sample powder were reacted in 1.5 ml of 2% HNO_3 solution for > 1 hour prior to analysis on a Thermo Scientific Element XR high-resolution inductively coupled plasma mass spectrometer (HR-ICP-MS) at the R. Ken Williams '45 Radiogenic Isotope Geosciences Laboratory at Texas A&M University. To correct for instrument drift, ~0.115 ml of 100 ppb indium standard was also added to each solution. Analytical sessions included measurements of internal standards with known elemental concentrations. Samples found with Mn^{2+} > 150 ppm or Fe^{2+} > 400 ppm were considered

as possibly diagenetically altered and were not used for paleotemperature calculations, but were included for burial history analysis.

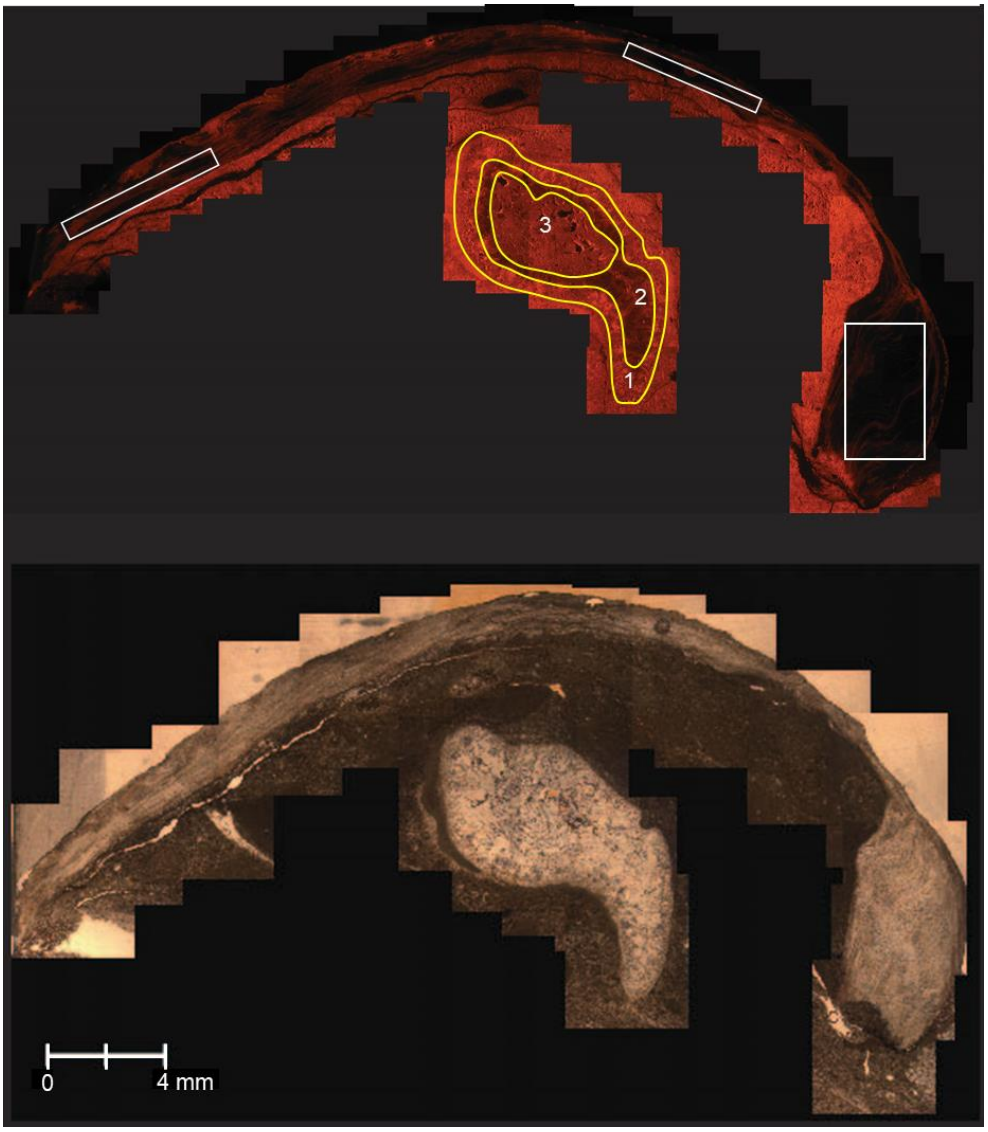

Figure 4. Cathodoluminescent images (top) and plane-light (bottom) photomicrographs of thin sections of *Hebertella* (MCH-1). White boxes indicate non-luminescent areas of the shell that was sampled. Numbered yellow polygons indicate multigenerational cements. Polygon 1 is the oldest cement, and polygon 3 is the youngest.

3.3. Sampling methods

Sample powders were collected using a New Wave micromill with a 0.5 mm diameter drill bit, and a dental drill with a 0.5 mm diameter drill bit. Sample sites were chosen from non-luminescent areas of shells based on the cathodoluminescence images of the thin sections (Grossman et al., 1996; Lee and Wan, 2000; Wefer and Berger, 1991). Multiple locations were sampled within some shells for replication purposes. Cement samples were extracted using a dental drill with a 0.5 mm diameter drill bit, and a New Wave micromill with a 0.5 mm diameter drill bit. Multi-generational cements were sampled starting from the outermost cements, which should be the oldest material, continuing inward to the central region, which should contain the youngest material. When possible, 2 mg of powder were recovered from the cements.

3.4. Isotopic Analyses

3.4.1. Clumped Isotopes

Eight to ten replicates of ~115 µg (1 to 1.5 mg) of powder from each cement and shell sample were reacted with "105 %" phosphoric acid in a Thermo Fisher Scientific Kiel IV carbonate device. The resultant CO_2 passed through a Porapak Q and silver wool trap cooled to -20 °C, designed to reduce possible carbon and sulfur compound contaminants. After July, 2020 the Porapak Q trap was cooled to -30 °C to further reduce possible contmination. The cleaned CO_2 was analyzed in a Thermo Fisher Scientific 253

Plus isotope ratio mass spectrometer in Long Integration Dual Inlet (LIDI) mode (Bernasconi et al., 2018; Grauel et al., 2013; Schmid and Bernasconi, 2010). The IRMS contains seven Faraday cups to measure m/z 44, 45, 46, 47, 48, 49, and 47.5. This array of Faraday cups allows for the simultaneous collection of $\delta^{13}C$, $\delta^{18}O$, and Δ_{47} measurements. The m/z 48 and 49 Faraday cups are used to check for contamination from carbon and sulfur compounds.

3.4.2. Clumped Data Processing

To address the complexities related to clumped carbonate isotopic measurements, the collected data, including carbonate standards and unknowns were inputted into Easotope, an open-source software tool developed specifically for clumped isotope data processing (John and Bowen, 2016). Easotope calculates $\delta^{18}O$, $\delta^{13}C$, and Δ_{47} values, the last within the "Carbon Dioxide Equilibrium Scale" (CDES) (Dennis et al., 2011). These corrections include acid digestion fractionation factors for both $\delta^{18}O$ (Kim et al., 2007) and Δ_{47} values (Petersen et al., 2019), ^{17}O correction (Brand et al., 2010), and non-linearity corrections related to the IRMS on which the analyses were performed (Dale et al., 2014; Meckler et al., 2014).

Replicates were screened using multiple protocols as a means of QA/QC. Replicates with a $\delta^{13}C$ or $\delta^{18}O$ value falling outside $\pm 2\sigma$ the mean of that sample were discarded regardless of the Δ_{47} value. Peirce's criterion was then used to determine outliers in the remaining Δ_{47} data set, which were then removed (Ross, 2003).

Clumped carbonate isotope (Δ_{47}) temperatures were calculated using the Kele et al. (2015) temperature calibration recalculated with the "Brand parameters" for ^{17}O correction (Brand et al., 2010) and the new accepted values for the ETH standards as reported in Bernasconi et al. (2018). This calibration was chosen because samples were measured and converted to the CDES using a similar methodology as those from this study. Also, this revised Kele et al. (2015) calibration is statistically indistinguishable from independent calibrations for marine biogenic and synthetic calcite from other laboratories (Jautzy et al., 2020; Meinicke et al., 2020; Peral et al., 2018), suggesting that it is appropriate for marine biogenic carbonates. The equation

$$\Delta_{47} = 0.0449\ (\pm 0.001) * 10^6/T^2 + 0.167\ (\pm 0.001) \quad (4)$$

where T is in kelvin will be referred to hereafter as the Bernasconi et al. (2018) temperature calibration.

To calculate the formation water compositions ($\delta^{18}O_{water}$), the clumped isotope temperatures were input into the calcite-H_2O fractionation relationship of Kim and O'Neil (1997).

$$1000\ln\alpha_{calcite\text{-}H2O} = 18.03(10^3/T) - 32.42 \quad (5)$$

where T is in kelvin.

For comparison, clumped isotope data from Bergmann et al. (2018) have been recalculated using the 90° C acid digestion fractionation factor from Petersen et al. (2019), and the Bernasconi et al. (2018) temperature calibration (eq. 4).

4. RESULTS

4.1. Petrographic and Cathodoluminescence Microscopy

The studied brachiopod shells display few to no fractures, and little to no evidence of recrystallization in plane-polarized light. Most brachiopod shells were sampled from non-luminescent areas identified in the cathodoluminescence images (figure 4). If non-luminescent areas were not present, samples were taken from slightly luminescent areas for comparison with internal cements, but were not taken into account for paleotemperature data due to alteration of the original isotopic signal (Popp et al., 1986).

In plane-polarized light, the first generation of internal cements occurs as light-brown turbid to translucent, bladed crystals and translucent, equant crystals while the later generation occurs as translucent equant crystals. All internal cements are luminescent, ranging from dull to bright orange; the intensity of luminescence varies considerably between each generation of cement but most individual generations of cement display a uniform luminescence. The first generation of cements occur as dull to bright luminescence bladed to equant crystals. None of the earliest generation of cements exhibit luminescence zoning. The second generation of cements occur as dull to bright orange equant crystals (figure 5).

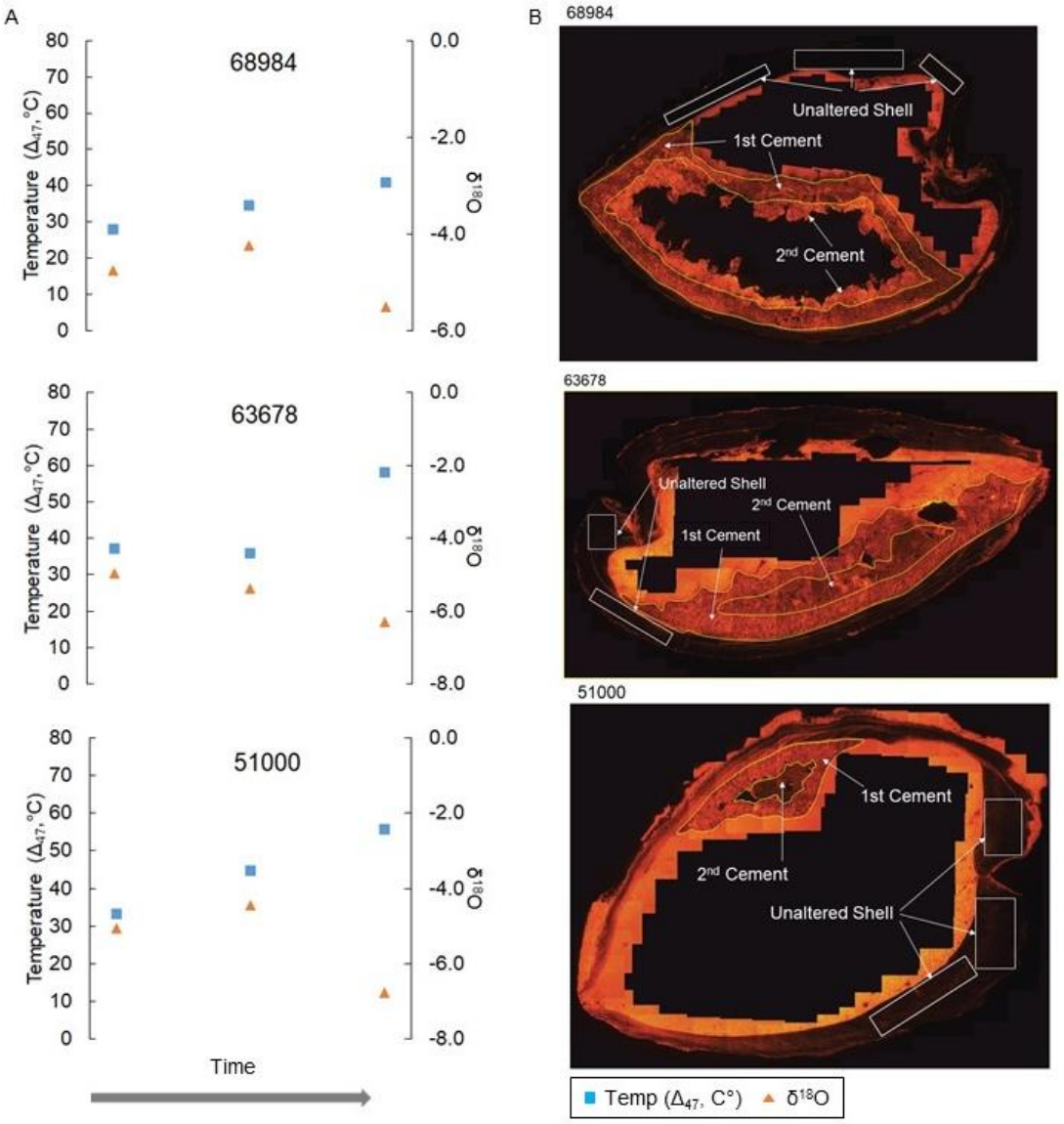

Figure 5. A) Clumped carbonate isotope temperatures, and $\delta^{18}O_{carb}$ of brachiopod shells (leftmost) and the internal multi-generational cements within the shell. Blue squares represent clumped carbonate isotope temperatures. Orange triangles represent $\delta^{18}O_{carb}$. Clumped carbonate isotopic temperatures were calculated using the Δ_{47} temperature calibration defined in Bernasconi et al. (2018). B) Cathodoluminescence images of brachiopod shells and internal multi-generational cements measured.

4.2. Brachiopod Shell and Clumped Isotopes

Table 1 shows the results isotopic analyses for brachiopod shells and calcitic cements. Included are $\delta^{13}C_{VPDB}$, $\delta^{18}O_{VPDB}$, and Δ_{47} composition, and calculated $\delta^{18}O_{water}$.

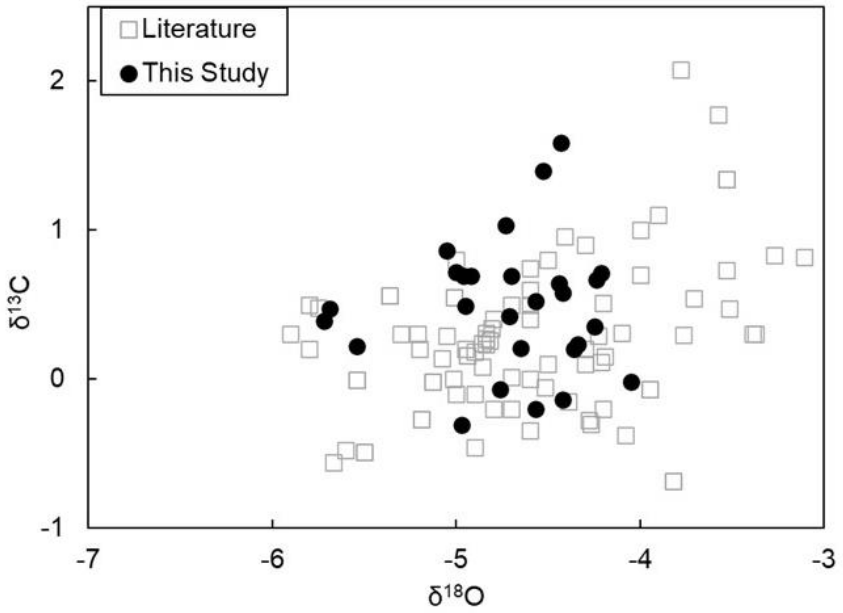

Figure 6. $\delta^{13}C$ vs $\delta^{18}O$ of calcitic brachiopods. Black circles represent specimens from this study. Gray squares represent specimens from Bergmann et al. (2018), Finnegan et al. (2011), Qing and Veizer, (1994), Shields et al. (2003), Veizer et al. (1999), and Wadleigh, and Veizer, (1992).

The carbon isotopic composition of Cincinnatian brachiopod shells ranges from -0.99 to 0.86‰, and the $\delta^{18}O_{VPDB}$ values range from -5.96 to -4.05‰. These results show no correlation between $\delta^{13}C_{VPDB}$ and $\delta^{18}O_{VPDB}$ (r^2= 0.0007) (figure 6) and are comparable to the results of previous studies of Late Ordovician fossils that also used

screening methods (i.e., cathodoluminescence, SEM, or trace element analyses) to identify the best-preserved brachiopod material (Shields et al., 2003; Qing and Veizer, 1994; Wadleigh and Veizer, 1992) (figure 7).

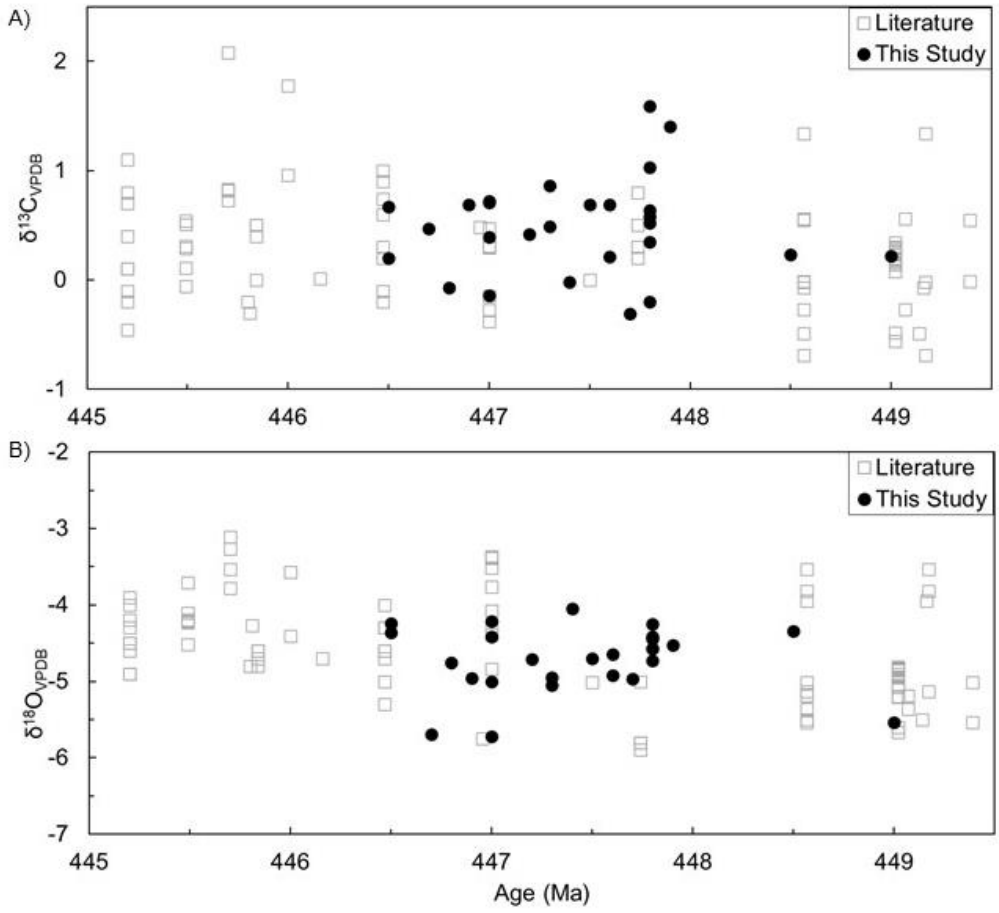

Figure 7. A) $\delta^{18}O$ of calcitic brachiopods vs age (Ma) B) $\delta^{13}C$ of calcitic brachiopods vs age (Ma). Black circles represent specimens from this study. Gray squares represent specimens from Bergmann et al. (2018), Finnegan et al. (2011), Qing and Veizer, (1994), Shields et al. (2003), Veizer et al. (1999), and Wadleigh, and Veizer, (1992).

Δ_{47} compositions for well-preserved, Cincinnatian brachiopod shells range from 0.568 to 0.669%, with an average measurement error of 0.017 (1SE). Δ_{47} temperatures calculated using the Bernasconi et al. (2018) equation (eq. 4) range from 25 to 61 °C (figure 12). These temperatures yield calculated $\delta^{18}O_{water}$ values of -2.9 to 4.8‰ VSMOW using calcite-H_2O fractionation relationship defined in Kim and O'Neil (1997) (eq. 5).

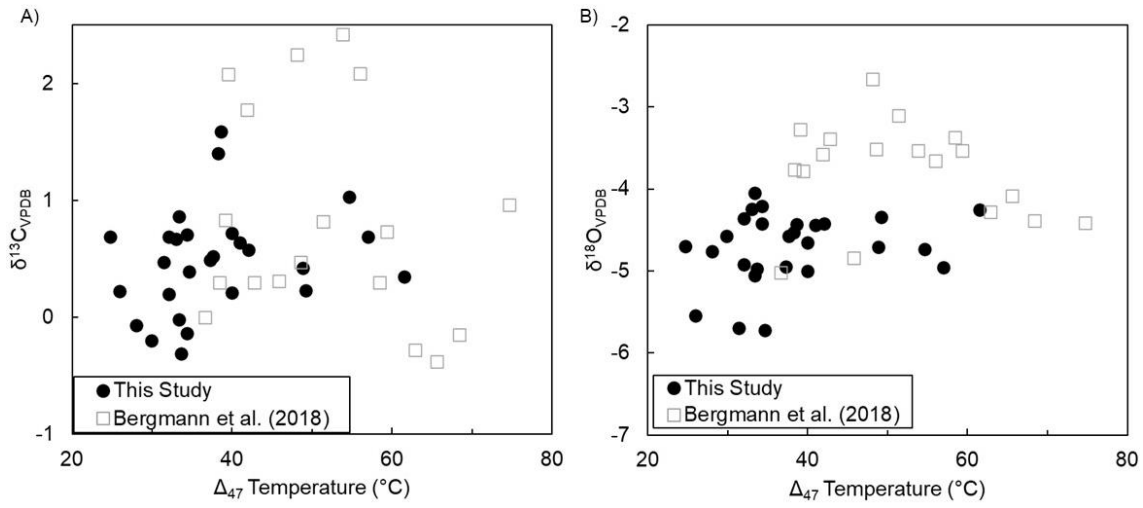

Figure 8. A) $\delta^{13}C_{VPDB}$ of calcitic brachiopods vs Δ_{47} temperature (°C) B) $\delta^{18}O_{VPDB}$ of calcitic brachiopods vs Δ_{47} temperature (°C). Black circles represent specimens from this study. Gray squares represent specimens from Bergmann et al. (2018).

Δ_{47} temperatures show no correlation with either $\delta^{13}C_{VPDB}$ or $\delta^{18}O_{VPDB}$ of the well-preserved brachiopod shells (r^2= 0.549, and 0.055 respectively)(figure 8). Data from this study displays tighter clustering when compared with data from Bergmann et al. (2018) is due to a higher number of low Δ_{47} temperatures in this study.

4.3. Cement Stable and Clumped Isotopes

The carbon isotopic composition of internal calcite cements ranges from -2.37 to 0.15‰. The $\delta^{18}O_{VPDB}$ for the cements range from -9.11 to -4.15‰. The first-generation cements display $\delta^{13}C_{VPDB}$ values lower than those of the brachiopod shells and $\delta^{18}O_{VPDB}$ values that are mostly similar(~1‰) to the best-preserved brachiopod shells. The second-generation cements are highly variable in both $\delta^{13}C_{VPDB}$ and $\delta^{18}O_{VPDB}$ (figure 9). This variability is suggestive on different precipitation environments for this generation of cements.

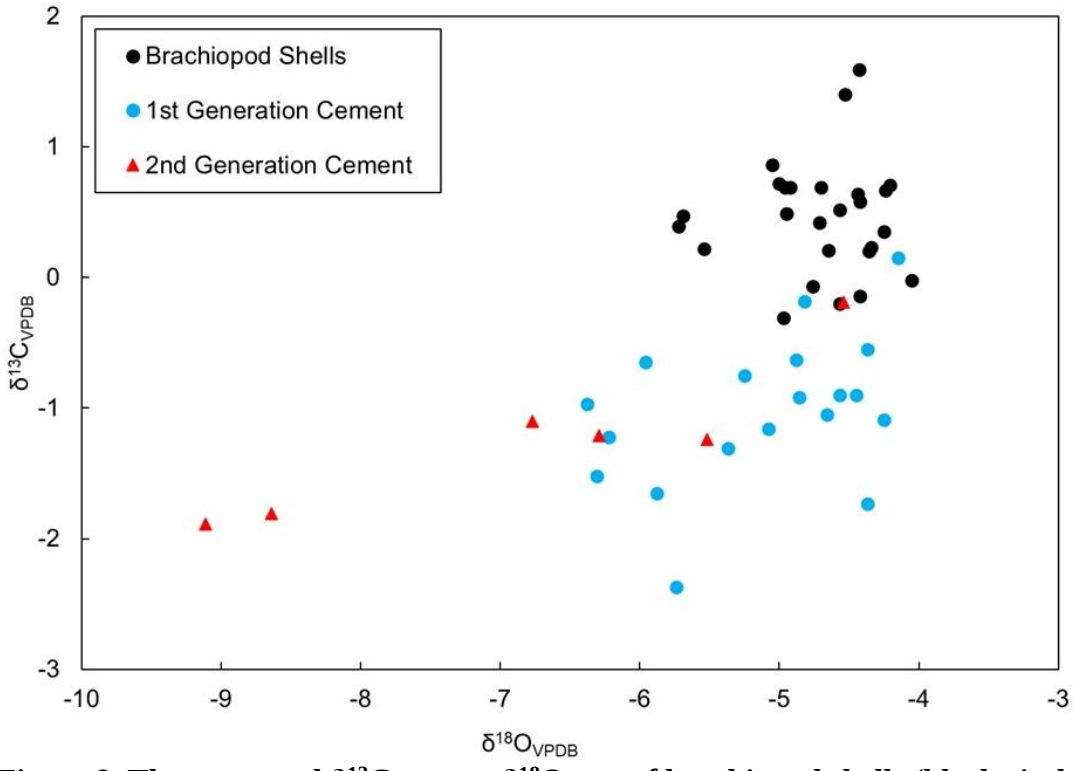

Figure 9. The measured $\delta^{13}C_{VPDB}$ vs. $\delta^{18}O_{VPDB}$ of brachiopod shells (black circles), the first generation of internal cements (blue circles), and the second generation of internal cements (red triangles).

Cement Δ_{47} values range from 0.517 to 0.701%, with an average measurement error of 0.019 (1SE). Δ_{47} temperatures calculated using the Bernasconi et al. (2018) equation (eq. 4) range from 17 to 85 °C. These temperatures yield calculated $\delta^{18}O_{water}$ values of -5.7 to 4.4‰ VSMOW using the relationship of Kim and O'Neil (1997) (eq. 5). Δ_{47} temperatures show no correlation with $\delta^{13}C_{VPDB}$ or $\delta^{18}O_{VPDB}$ of the first-generation cements (r^2= 0.1, and 0.056 respectively). Likewise, $\delta^{13}C_{VPDB}$ and $\delta^{18}O_{VPDB}$ show no correlation with the second-generation cements (r^2= 0.16 and 0.2, respectively) (figure 10A). Many of the first-generation cements display higher Δ_{47} temperatures than best-preserved brachiopod shells while having similar $\delta^{18}O_{VPDB}$ while the second generation of cements display a high degree in variability in both Δ_{47} temperature and $\delta^{18}O_{VPDB}$ (figure 10B).

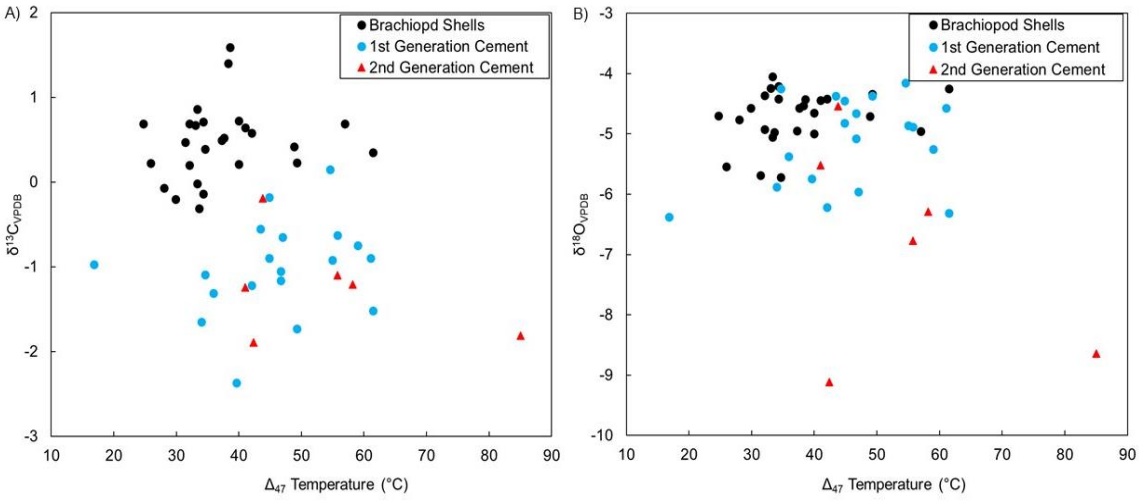

Figure 10. A) $\delta^{13}C$ of calcitic cements vs Δ_{47} temperature (°C) B) $\delta^{18}O$ of calcitic cements vs Δ_{47} temperature (°C). Black circles represent specimens from this study. Blue circles represent first generation of cements, and red triangles represent the second generation of cements.

Table 1. Isotopic composition of analyzed brachiopods and internal cements (‰)

Sample	Material	Age (Ma)	$\delta^{13}C_{VPDB}$	1SE	$\delta^{18}O_{VPDB}$	1SE	$\Delta_{47\ CDES25}$	1SE	T (°C)*	1SE	$\delta^{18}O_{H_2O\ VSMOW}$**	1SE
65983	Brachiopod	443.5	0.64	0.01	-4.27	0.01	0.588	0.012	53	4	3.4	0.7
OKP-1	Brachiopod	446.5	0.67	0.01	-4.24	0.01	0.646	0.015	33	4	-0.3	0.9
OKH-1	Brachiopod	446.5	0.2	0.02	-4.36	0.03	0.649	0.021	32	6	-0.6	1.2
OKH-1-C	Cement		-0.18	0.01	-4.82	0.01	0.611	0.02	45	6	1.4	1.2
66378	Brachiopod	446.7	0.47	0.01	-5.69	0.01	0.651	0.011	31	3	-2.0	0.7
66378-C	Cement		-0.55	0.00	-4.37	0.02	0.615	0.013	43	4	1.6	0.8
27542	Brachiopod	446.7	-0.5	0.03	-4.69	0.02	0.661	0.017	28	5	-1.6	1.0
27542-C	Cement		-1.16	0.02	-5.08	0.02	0.606	0.024	47	7	1.4	1.4
68984	Brachiopod	446.8	-0.07	0.02	-4.76	0.02	0.662	0.023	28	7	-1.86	1.4
68984-C1	Cement - 1st		-1.09	0.01	-4.25	0.02	0.641	0.025	35	7	0.0	1.5
68984-C2	Cement - 2nd		-1.24	0.01	-5.52	0.02	0.622	0.019	41	6	0.0	1.1
CCSP-1	Brachiopod	446.9	0.69	0.01	-4.96	0.02	0.579	0.015	57	4	3.3	0.9
CCSP-2	Brachiopod	446.9	-0.5	0.01	-4.75	0.03	0.631	0.019	38	6	0.2	1.1
CCSP-2-C	Cement		-1.52	0.01	-6.31	0.05	0.568	0.013	61	4	2.7	0.8
27638	Brachiopod	447	0.71	0.01	-4.21	0.02	0.642	0.016	34	5	0.0	0.9
27638-C1	Cement - 1st		-1.81	0.01	-8.64	0.01	0.517	0.018	85	5	3.9	1.1
27638-C2	Cement - 2nd		-1.05	0.01	-4.66	0.01	0.606	0.019	47	6	1.8	1.1
2142-1	Brachiopod – Interior	447	0.39	0.01	-5.72	0.01	0.641	0.026	35	8	-1.4	1.5
2142-2	Brachiopod - Exterior	447	0.72	0.01	-5	0.02	0.625	0.019	40	6	0.3	1.1
27724	Brachiopod	447	-0.14	0.01	-4.42	0.02	0.642	0.011	34	3	-0.2	0.7
27724-C	Cement		-0.90	0.01	-4.57	0.02	0.569	0.020	61	6	4.4	1.2
51149	Brachiopod	447.2	0.42	0.01	-4.71	0.01	0.600	0.011	49	3	2.2	0.7
51149-C	Cement		-0.92	0.00	-4.86	0.01	0.584	0.014	55	4	3.1	0.8
51000	Brachiopod	447.3	0.86	0.02	-5.05	0.02	0.645	0.027	33	8	-1.0	1.6
51000-C1	Cement - 1st		-0.9	0.02	-4.45	0.02	0.611	0.022	45	6	1.7	1.3
51000-C2	Cement - 2nd		-1.1	0.01	-6.77	0.03	0.582	0.040	56	12	1.3	2.4
63678	Brachiopod	447.3	0.49	0.01	-4.95	0.02	0.633	0.020	37	6	-0.2	1.2
63678-C1	Cement – 1st		-1.31	0.01	-5.37	0.02	0.637	0.023	36	7	-0.8	1.4
63678-C2	Cement – 2nd		-1.21	0.01	-6.29	0.06	0.576	0.018	58	5	2.2	1.1
69459	Brachiopod	447.4	-0.02	0.00	-4.05	0.01	0.645	0.011	33	3	0.0	0.7
69459-C	Cement		-1.73	0.01	-4.37	0.01	0.599	0.011	49	3	2.6	0.7

Table 1. Continued

Sample	Material	Age (Ma)	$\delta^{13}C_{VPDB}$	1SE	$\delta^{18}O_{VPDB}$	1SE	$\Delta_{47\ CDES25}$	1SE	T (°C)*	1SE	H_2O $\delta^{18}O_{VSMOW}$**	1SE
78682	Brachiopod	447.5	0.69	0.01	-4.7	0.01	0.673	0.029	25	9	-2.35	1.7
78682-C	Cement		-1.65	0.01	-5.88	0.04	0.643	0.029	34	9	-1.72	1.7
63696	Brachiopod	447.6	0.21	0.01	-4.65	0.01	0.625	0.014	40	4	0.6	0.8
63696-C1	Cement – 1st		-2.37	0.01	-5.74	0.03	0.626	0.014	40	4	-0.5	0.8
63696-C2	Cement – 2nd		-1.89	0.01	-9.11	0.02	0.618	0.014	42	4	-3.4	0.8
78700	Brachiopod	447.6	0.69	0.01	-4.92	0.01	0.649	0.021	32	6	-1.1	1.2
27909-1	Brachiopod - Interior	447.7	-0.31	0.01	-4.97	0.01	0.644	0.020	34	6	-0.9	1.2
27909-2	Brachiopod - Exterior	447.7	-1.01	0.02	-5.97	0.02	0.651	0.029	31	9	-2.3	1.7
27921	Brachiopod	447.8	0.58	0.02	-4.42	0.01	0.619	0.019	42	6	1.3	1.1
27921-C	Cement		-1.22	0.01	-6.22	0.02	0.619	0.017	42	5	-0.6	1.0
MCP-1	Brachiopod - Interior	447.8	0.64	0.01	-4.44	0.01	0.622	0.017	41	5	1.0	1.0
MCP-1-C	Brachiopod - Exterior	447.8	0.35	0.01	-4.25	0.01	0.568	0.012	61	4	4.8	0.7
MCP-5	Brachiopod	447.8	0.52	0.01	-4.57	0.01	0.632	0.016	38	5	0.3	0.9
MCP-5-C	Cement		-0.65	0.01	-5.96	0.03	0.605	0.015	47	4	0.6	0.8
MCH-1	Brachiopod	447.8	-0.2	0.01	-2.57	0.01	0.656	0.024	30	7	-1.2	1.4
MCH-1-C1	Cement – 1st		0.15	0.01	-4.15	0.01	0.585	0.026	55	8	3.7	1.5
MCH-1-C2	Cement – 2nd		-0.19	0.02	-4.54	0.04	0.614	0.013	44	4	1.7	0.8
MCH-3	Brachiopod	447.8	-0.06	0.01	-4.59	0.01	0.629	0.019	39	6	0.4	1.1
27969	Brachiopod	447.8	1.59	0.01	-4.43	0.01	0.629	0.018	39	5	0.6	1.1
27969-C	Cement		-0.63	0.01	-4.88	0.02	0.582	0.017	56	5	3.2	1
68818	Brachiopod	447.9	1.4	0.01	-4.53	0.01	0.630	0.014	38	4	0.4	0.8
68980	Brachiopod	448.5	0.23	0.02	-4.34	0.01	0.599	0.015	49	4	2.6	0.9
68980-C	Cement		-0.97	0.01	-6.38	0.08	0.701	0.029	17	9	-5.67	1.7
68766	Brachiopod	449	0.22	0.01	-5.54	0.01	0.669	0.020	26	6	-2.9	1.2
68766-C	Cement		-0.75	0.01	-5.25	0.04	0.574	0.009	59	3	3.3	0.5

*Calculated using Bernasconi et al. (2018) temperature calibration

**Calculated using Kim and O'Neil (1997) calcite-H_2O relationship

5. DISCUSSION

5.1. Brachiopod Δ_{47} paleotemperatures and $\delta^{18}O$ of Late Ordovician seawater

The Δ_{47} temperatures of brachiopod shells from this study range from 25 - 61°C with a mean of 38 °C, and median of 36 °C, while the Δ_{47} temperature of Laurentian brachiopod shells from Bergmann et al. (2018) range from 30 - 64 °C with a mean of 44 °C, and median of 41 °C.

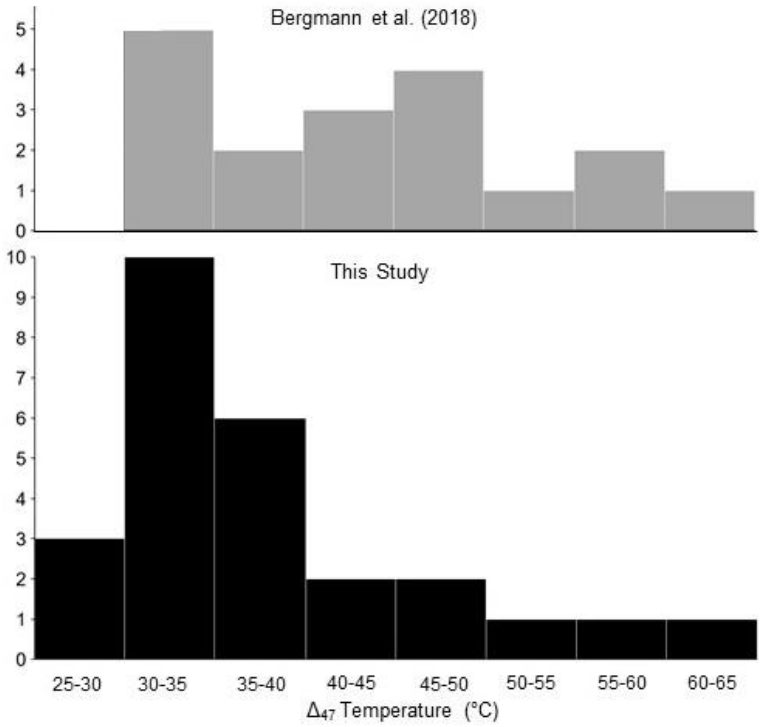

Figure 11. Histograms comparing brachiopod Δ_{47} temperatures from Bergmann et al. (2018) (gray) and this study (black).

The Δ_{47} temperatures of brachiopod shells from this study display a skewed-right quasi-lognormal distribution (89% probability as determined by Prism™ using the

method of Burnham and David, 2002) with strong mode at 30 - 35 °C opposed to data from Bergmann et al. (2018) which displays a weak lognormal distribution (63% probability) with a mode at 41 °C. The lower temperatures and development of a strong mode in these data at T=30 - 35 °C can be attributed to the ability to target only the best-preserved portions of the shell afforded by the smaller sample size required for this method compared with the larger sample sizes of previous studies (Bernasconi et al., 2018; Schmid and Bernasconi, 2010). However, even using the best-preserved material, the tail in the quasi-lognormal distribution suggest partial reordering of some of the brachiopod shells in both datasets.

This partial reordering, despite minimal burial heating, suggests that the reordering process is not uniform in nature, but occurs as a disordered kinetic process where solid state C–O isotope exchange occurs as a multiple, parallel first-order reactions each with a different activation energies (Hemingway and Henkes, 2020). This disordered kinetic process is similar to the processes used to describe the of pyrolysis of biomass into coal. Pyrolysis of biomass is often modeled using a distribution activation energy model (DAEM) (Cai et al., 2014; Please et al., 2003). When applied to clumped bond reordering, this model assumes the declumping mechanisms occur as independent, parallel, first-order reactions with different activation energies. The difference in activation energies can be represented by a continuous distribution function (Hemingway and Henkes, 2020).

At the present there is no known way to deconvolve the different mechanisms that caused the partial reordering of some of the brachiopod shells; however, interpretation of

the brachiopod paleotemperature data has been limited to the brachiopod shells within the modal bin of 30 -35 °C (figure 11). To determine if these and Bergmann et al.'s (2018) data are statistically different, a Mann-Whitney test was performed, giving a p-value of 0.08. While this is not significant to the 95%, it is significant to the 90% indicating that it is probable that the datasets are statistically different.

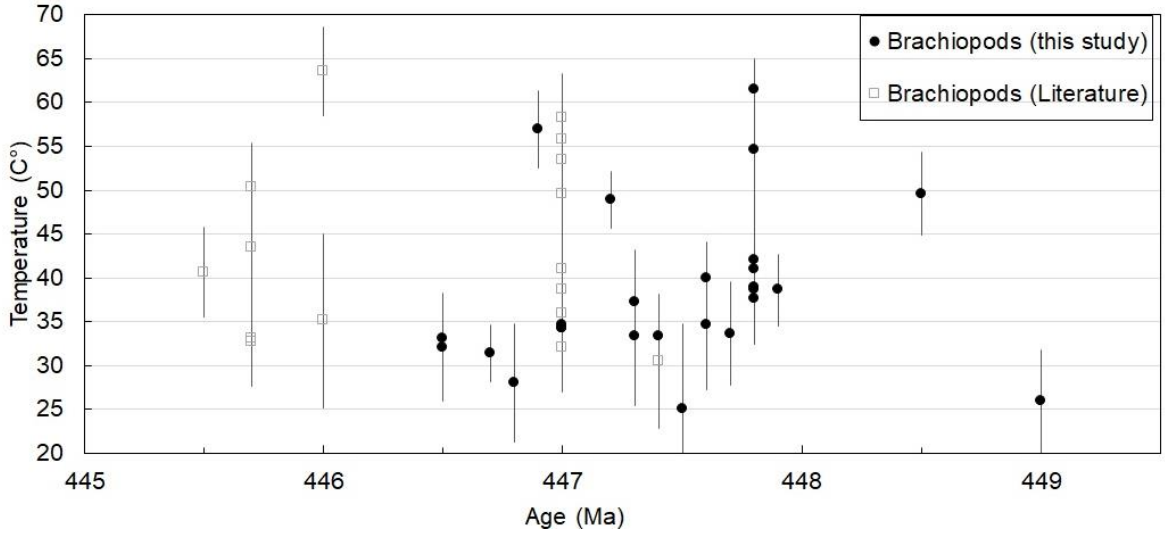

Figure 12. Compilation of Δ_{47} temperatures (±1SE) vs. age for brachiopod shells from this study and Bergmann et al. (2018). Black circles are data from this study. Gray squares are data from previous studies. Clumped carbonate isotopic temperatures were calculated using the Δ_{47} temperature calibration of Bernasconi et al. (2018).

These modal Δ_{47} temperatures are equal to or slightly higher than sea surface temperatures in the modern West Pacific Warm pool (30-35 °C vs. ~30°C) (De Deckker, 2016) and also do not exceed the maximum temperature for growth of 41 °C put forward by Storch et al., (2014) (figure 12). The data suggest a relatively stable climate for most

of the studied interval. These temperatures are similar to those found by other studies of Phanerozoic greenhouse climates such as the Paleocene Eocene Thermal Maximum (PETM) and the late Cenomanian and Turonian stages (~33 °C, and ~35-36°C, respectively) (Frieling et al., 2017; Forster et al., 2007; Sluijs et al., 2011). These temperatures also may reflect seasonal biases towards warmer growth periods (Butler et al., 2015) or may reflect local seawater conditions due to the unique hydrography of epicontinental seas. Epicontinental seas are shallower and more confined than the open ocean allowing for surface waters to change temperature more rapidly than a deep ocean basin at the same latitude (~2-4 °C) (Judd et al., 2020); however, studies have suggested the carbonate platforms of the Cincinnati Arch were not solely influenced by the warmer epicontinental shelf waters. Evidence based on stratigraphic analysis of the region suggests that cold phosphate-rich deep water from the Iapetus Ocean moved northward through the Sebree trough, upwelling, and mixing with the warm oxygen-rich waters of the epicontinental sea at the Cincinnati Arch (Kolata et al., 2001) (figure 13). The presence of cool-water carbonates (e.g. abundant bryozoan-brachiopod-echinoderm grain- and packstones, and an abundance of marine cemented and phosphatized hardgrounds) on the Cincinnati Arch while at 25-30°S latitude also suggests a cool-water source influencing the region (Pope and Read, 1997, 1998). This interaction allows for an environment that would more closely reflect the chemical composition of the global ocean instead of the local conditions of the epicontinental sea.

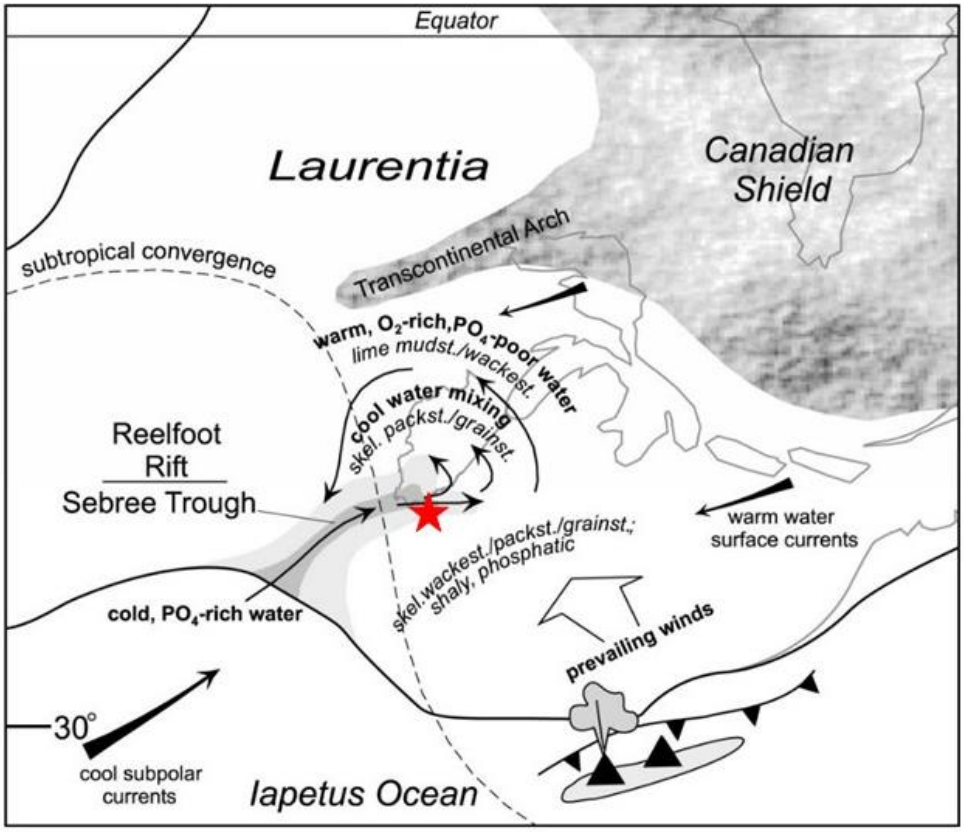

Figure 13. Late Ordovician paleogeography of Laurentia showing tectonic features, atmospheric and oceanic circulation patterns, lithofacies, and water masses in the Midcontinent seaway. Red star indicates study area. Adapted from Kolata et al., (2001).

Using the modal brachiopod Δ_{47} temperatures above, calculated seawater $\delta^{18}O$ values range from -2.0 to 0.8 ‰ with an average of -0.5 ±1.1‰VSMOW over the studied interval (figure 14). These results echo results from previous clumped isotope studies that the seawater $\delta^{18}O$ has not changed more than ± 1‰ throughout the Phanerozoic era, and that the secular trend seen in the $\delta^{18}O$ of carbonate fossils is a product of higher temperatures during the early Paleozoic with cooling towards the modern (Bergmann et al., 2018; Came et al., 2007; Finnegan et al., 2011; Henkes et al., 2018). The results also

agree with results from studies of ophiolites, hydrothermal alteration of the seafloor, and $\delta^{18}O$ of marine iron oxide which also suggest little change in seawater $\delta^{18}O$ throughout the Phanerozoic (Galili et al., 2019; Hodel et al., 2018; Lécuyer et al., 1995; Muehlenbachs, 1998; Muehlenbachs et al., 2003).

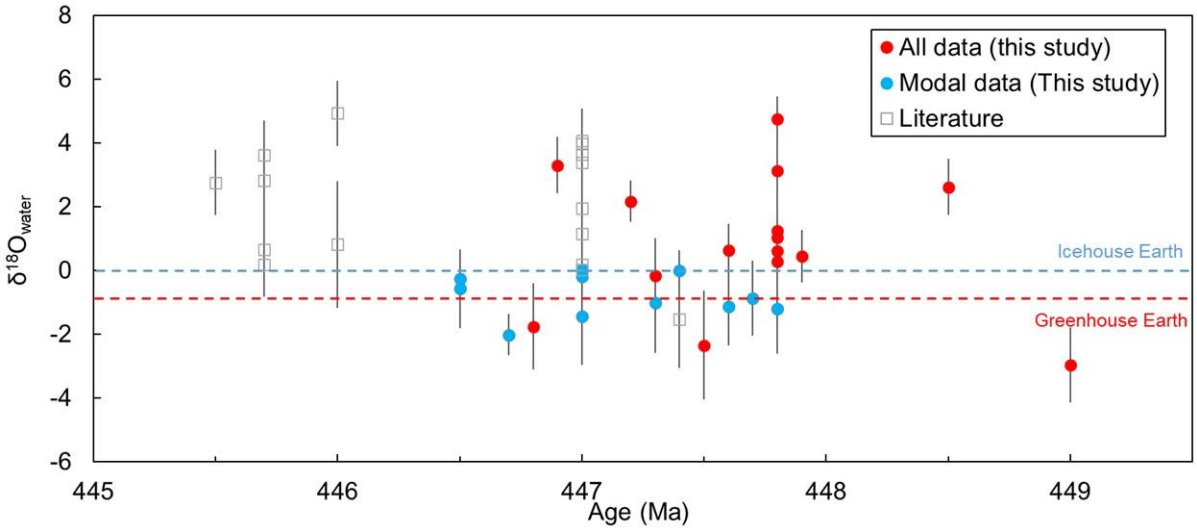

Figure 14. Calculated $\delta^{18}O_{water}$ (±1SE) vs. Age (Ma) for this study. Blue dashed line indicates $\delta^{18}O$ of seawater in an Icehouse Earth similar to today. Red dashed line indicated $\delta^{18}O$ of seawater in Greenhouse Earth. Blue circles indicate calculated $\delta^{18}O_{water}$ from the strong modal data (30-35 °C) from this study. Blue circles indicate all calculated $\delta^{18}O_{water}$ outside of the strong modal bin from this study. Gray squares indicate calculated $\delta^{18}O_{water}$ from Bergmann et al. (2018). $\delta^{18}O_{water}$ values were calculated using the calcite-H_2O ^{18}O fractionation relationship of Kim and O'Neil (1997).

5.2. Cement Δ_{47} temperatures and burial history

Calcitic cements have long been used as proxies of oceanographic and diagenetic conditions during cementation of carbonate materials (Given and Lohmann, 1985;

Lohmann and Walker, 1989; Tobin and Walker, 1997). In many studies, petrographic fabrics have been the main, and sometime sole, criteria used to determine precipitation environment; however, multiple studies have shown that petrographic fabrics should not be used as the sole indicator of precipitation environment(Kendall, 1985; Tobin and Walker, 1996; Wilkinson et al., 1985; Wilson and Palmer, 1992). Similar petrographic fabrics can precipitate in different environments depending on the chemistry of the precipitating fluid, thus are unreliable proxies for precipitation environment. Along with petrographic fabrics, stable isotopes, cathodoluminescence, and trace element analysis should be used as proxies to give insight into precipitation environments for calcitic cements (Kendall, 1985; Kim and Lee, 1996; Melim et al., 1995; Saller and Moore, 1991; Tobin and Walker, 1997; Tobin et al., 1999; Wilkinson et al., 1982, 1985; Wilson and Palmer, 1992). More recently Δ_{47} temperatures of calcitic cements have proved invaluable constraints the burial and diagenetic temperature history of sediment packages(Huntington et al., 2011; Shenton et al., 2015).

The first generations of internal cements from these Late Ordovician brachiopods show uniform cathodoluminescence and mostly yield $\delta^{18}O$ (figure 9) values similar to those of the best-preserved brachiopod fossils, indicating that these cements formed in a marine setting (Kendall, 1985; Marshall and Middleton, 1990; Tobin and Walker, 1996, 1997; Wilkinson et al., 1982, 1985). Thus, these cements should retain isotopic signature of the original precipitation environment, including $\delta^{13}C$, $\delta^{18}O_{VPDB,}$ Δ_{47}; however, based on the Δ_{47} temperatures, many of the first-generation of internal cements show some degree of partial reordering with higher temperatures than the shells. This makes the

cements an unusable proxy for Late Ordovician marine environmental conditions, but they can still help constrain the burial and diagenetic history of the fossils and sedimentary packages.

Each generation of cement provides a Δ_{47} temperature "snapshot" of a diagenetic or burial condition, allowing the creation of a simple, burial history using the cement stratigraphy within the macropore of the articulated brachiopod shell. Δ_{47} temperatures of the brachiopod shells and cements show an increasing trend through time, while the $\delta^{18}O_{carb}$ of the same brachiopod shells and each sequential generation of internal cements show a decreasing trend through time (Figure 5). These trends suggest increasing burial for each generation of cement and reflect the diagenetic conditions at the time of precipitation. Using an average geothermal gradient (25 °C/km), one of the second-generation cements indicates a minimum burial depth of 2.4 km after deposition, which possibly occurred during the Carboniferous period. This proposed burial depth is deeper than previous studies have indicated (<1 to 2 km) (Epstein et al., 1977; Harris et al., 1978; Ryder, 1987).

5.3. Reordering rates of different phases of calcitic material

Based on burial estimates from the literature (Epstein et al., 1977; Harris et al., 1978; Ryder, 1987), and Δ_{47} temperatures of cements from this study, the brachiopods and cements did not reach the threshold temperature of 100° C to begin reordering the clumped carbonate bonds (Hemingway and Henkes, 2020; Henkes et al., 2014; Stolper and Eiler, 2015; Stolper et al., 2018). However, the higher Δ_{47} temperatures and higher

calculated $\delta^{18}O_{H2O}$ for the cements and some brachiopod shells, while having $\delta^{18}O_{carb}$ values similar to the modal brachiopod shells, are indicative of partial solid-state reordering (figure 15). The positive correlation between Δ_{47} temperature and $\delta^{18}O_{H2O}$ is diagnostic of rock-buffered diagenesis and solid-state reordering (Huntington and Lechler, 2015). This suggests that the calcite cements and some of the brachiopod shells began reordering at a lower temperature than the majority of the brachiopod shells.

There are two possible hypotheses to address this discrepancy: 1) previous studies have underestimated the burial depth of materials, or 2) another factor allows for the clumped carbonate bond to reorder before reaching the threshold temperature of 100 °C published in previous works (Hemingway and Henkes, 2020; Henkes et al., 2014; Stolper and Eiler, 2015; Stolper et al., 2018).

While it is possible that greater heat was applied to the fossils and cements than previous basin history studies have suggested, the data suggest that the required threshold temperature of ~100 °C was not reached (Epstein et al., 1977; Harris et al., 1978; Ryder, 1987), otherwise all of the marine materials would have similar Δ_{47} temperatures and thus show similar degree of partial reordering as opposed to only some of the shells and most of the marine cements showing these effects.

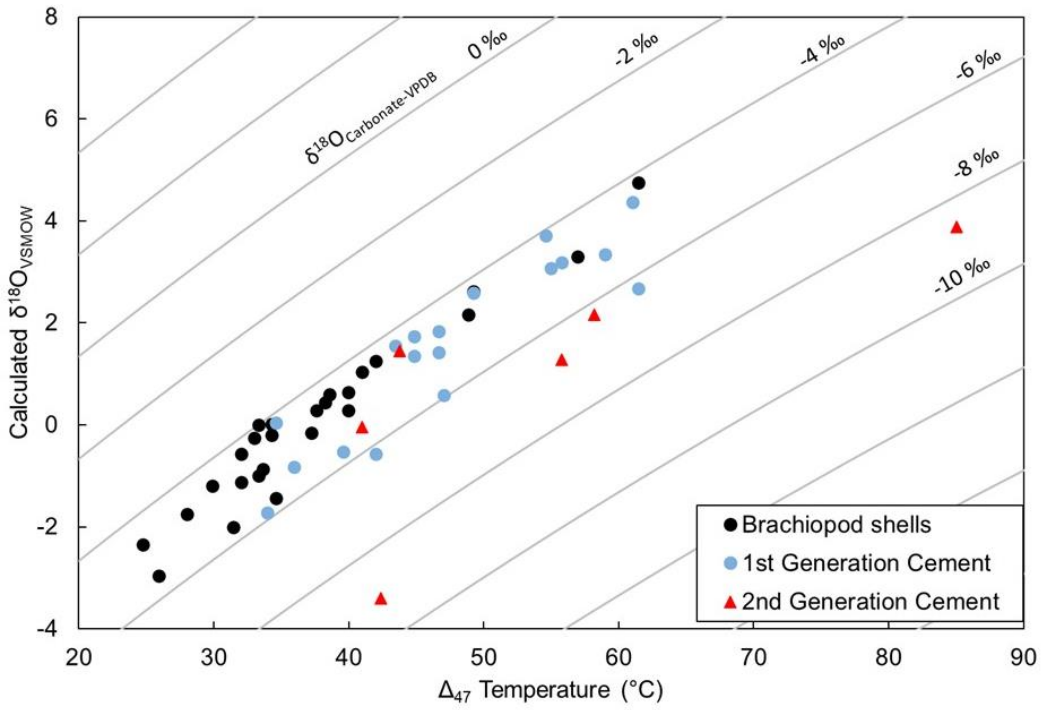

Figure 15. Calculated $\delta^{18}O_{VSMOW}$ vs. Δ_{47} temperature. Black circles indicated brachiopod shells. Blue circles indicate 1st generation of calcite cements. Red triangles indicate the 2nd generation of calcite cements. Gray contours lines indicate constant carbonate $\delta^{18}O_{VPDB}$ using the calcite-H_2O fractionation relationship of Kim and O'Neil (1997). The positive correlation between Δ_{47} temperature and water $\delta^{18}O_{VSMOW}$ is diagnostic of rock-buffered diagenesis and/or solid-state reordering (Huntington and Lechler, 2015).

A proposed mechanism for the increased reordering rate in some of the calcitic materials was put forth in Passey and Henkes (2012) and Henkes et al. (2014). Crystallographic defects within different phases of calcite caused by trace elements within the crystal lattice could control the calcitic phase's susceptibility or resistance to reordering. These crystallographic defects could provide locations where the oxygen atoms could diffuse more easily through the lattice facilitating reordering at temperatures below published thresholds. A similar, positive relationship between Mn content and the

rate of oxygen diffusion into the crystal lattice of calcite was identified in Kronenberg et al. (1984). However, the self-diffusion of carbon and oxygen through a carbonate mineral has been largely unexplored (Henkes et al., 2014). Henkes et al., (2014) noted that the experimentally heated calcite spar (NE-CC-1) from Passey and Henkes, (2012) displayed distinctly different reordering kinetics along with very different Mg and Mn contents when compared with the optical calcite and a well-preserved Permian brachiopod shell. This cement showed a very rapid initial reordering rate followed by a slower rate similar to the optical calcite and a well-preserved Permian brachiopod shell. The authors hypothesized that trace element concentrations in the cement caused the difference in reordering rates, allowing different phases of the calcitic material to be more susceptible to reordering. This same effect is most likely influencing the cements from this study. Based on cathodoluminescence, the cements have higher concentrations of Mn than the well-preserved brachiopods causing these Mn-rich phases to be more susceptible to reordering than the well-preserved brachiopods, which are non-luminescent and thus lower in Mn content. Experimental studies are required to fully understand the relationship between crystallographic defects caused by trace elements, substitution and reordering kinetics in different calcitic phases.

6. CONCLUSION

Targeting small, well-preserved areas of shells resulted in slightly lower average Δ_{47} brachiopod temperatures using these smaller sample sizes compared with previous studies using larger samples (38 °C from this study vs. 44 °C from Bergmann et al., 2018). This method also resulted in a log-normal distribution with a strong mode at 33 °C as opposed to the weak log-normal distribution and higher modal temperature of 41 °C seen in the Bergmann et al. (2018) data. The modal Δ_{47} temperatures from this study are equal to or slightly higher than temperatures in the modern Western Pacific Warm Pool (30-35 ° C vs ~30 ° C). Modal temperatures from this study are also below maximum metazoan temperature for growth of 41 °C put forth by Storch et al. (2014) . Calculated $\delta^{18}O_{H2O}$ of the brachiopods echo previous studies suggesting that seawater $\delta^{18}O$ has not changed more than ± 1‰ throughout the Phanerozoic and that the trend seen in the $\delta^{18}O$ of carbonate fossils is a product of higher temperatures during the early Paleozoic with cooling towards the modern.

Smaller sample sizes allowed targeting of individual generation of cements within the brachiopod shells with a lower probability of mixing between the individual generations of cement. These data combined with the cement stratigraphy to better constrain the burial and diagenetic temperature history of the Cincinnati Group. The higher Δ_{47} temperature (85 °C) for cements from this study suggest minimum burial to a depth of 2.4 km compared with <1 to 2 km suggested by previous studies.

Δ_{47} temperatures from marine cements and some brachiopod shells show signs of partial reordering even though the materials did not reach the reordering threshold

temperature of 100° C. This implies that the chemistry of different phases of calcitic materials (e.g., phases rich in Mn) can have different reordering rates. Data from this study and others (Henkes et al., 2014) suggest that the chemistry of the calcitic materials can affect the reordering rate. Future studies should focus on the relationship between reordering rates and these crystallographic defects to better understand the reordering of the clumped carbonate signal.

REFERENCES

Aucoin, C.D., and Brett, C.E., 2015, Refined stratigraphy of the Late Ordovician (Katian; Richmondian) Waynesville Formation across the northeastern and northwestern margin of the Cincinnati Arch: Stratigraphy, v. 12.

Bergmann, K.D., Finnegan, S., Creel, R., Eiler, J.M., Hughes, N.C., Popov, L.E., and Fischer, W.W., 2018, A paired apatite and calcite clumped isotope thermometry approach to estimating Cambro-Ordovician seawater temperatures and isotopic composition: Geochimica et Cosmochimica Acta, v. 224, p. 18–41, doi: 10.1016/j.gca.2017.11.015.

Bergström, S.M., Young, S., and Schmitz, B., 2010, Katian (Upper Ordovician) $\delta^{13}C$ chemostratigraphy and sequence stratigraphy in the United States and Baltoscandia: A regional comparison: Palaeogeography, Palaeoclimatology, Palaeoecology, v. 296, p. 217–234, doi: 10.1016/J.PALAEO.2010.02.035.

Bernasconi, S.M., Müller, I.A., Bergmann, K.D., Breitenbach, S.F.M., Fernandez, A., Hodell, D.A., Jaggi, M., Meckler, A.N., Millan, I., and Ziegler, M., 2018, Reducing Uncertainties in Carbonate Clumped Isotope Analysis Through Consistent Carbonate-Based Standardization: Geochemistry, Geophysics, Geosystems, doi: 10.1029/2017GC007385.

Brand, W.A., Assonov, S.S., and Coplen, T.B., 2010, Correction for the ^{17}O interference in $\delta^{13}C$ measurements when analyzing CO_2 with stable isotope mass spectrometry (IUPAC Technical Report): Pure and Applied Chemistry, v. 82, p. 1719–1733, doi: 10.1351/PAC-REP-09-01-05.

Brand, U., Jiang, G., Azmy, K., Bishop, J., and Montañez, I.P., 2012, Diagenetic evaluation of a Pennsylvanian carbonate succession (Bird Spring Formation, Arrow Canyon, Nevada, U.S.A.) — 1: Brachiopod and whole rock comparison: Chemical Geology, v. 308–309, p. 26–39, doi: 10.1016/J.CHEMGEO.2012.03.017.

Brand, U., and Veizer, J., 1980, Chemical Diagenesis of a Multicomponent Carbonate System-1: Trace Elements: Journal of Sedimentary Petrology, v. 50, p. 1219–1236, http://citeseerx.ist.psu.edu/viewdoc/download?doi=10.1.1.857.865&rep=rep1&type=pdf (accessed July 2019).

Brenchley, P.J., Carden, G.A., Hints, L., Kaljo, D., Marshall, J.D., Martma, T., Meidla, T., and Nõlvak, J., 2003, High-resolution stable isotope stratigraphy of Upper Ordovician sequences: Constraints on the timing of bioevents and environmental changes associated with mass extinction and glaciation: Geological Society of America Bulletin, v. 115, p. 89–104, doi: 10.1130/0016-7606(2003)115<0089:HRSISO>2.0.CO;2.

Brenchley, P.J., Marshall, J.D., Carden, G.A.F., Robertson, D.B.R., Long, D.G.F., Meidla, T., Hints, L., and Anderson, T.F., 1994, Bathymetric and Isotopic Evidence for a Short-Lived Late Ordovician Glaciation in a Greenhouse Period: Geology, v. 22, p. 295–298, doi: Doi 10.1130/0091-7613(1994)022<0295:Baiefa>2.3.Co;2.

Brett, C.E., Mclaughlin, P.I., Schramm, T.J., Sullivan, N.B., Thomka, J.R., and Cramer, B.D., 2012, Middle Paleozoic Sequence Stratigraphy and Paleontology of the Cincinnati Arch : Part 1 Central Kentucky and Southern Ohio: IGCP Project 591,.

Buggisch, W., Joachimski, M.M., Lehnert, O., Bergström, S.M., Repetski, J.E., and Webers, G.F., 2010, Did intense volcanism trigger the first late Ordovician icehouse? Geology, v. 38, p. 327–330, doi: 10.1130/G30577.1.

Burnham, K., and David, A., 2002, Model selection and multimodel inference: a practical information-theoretic approach: Springer-Verlag New York, doi: 10.1007/b97636.

Butler, S., Bailey, T.R., Lear, C.H., Curry, G.B., Cherns, L., and McDonald, I., 2015, The Mg/Ca–temperature relationship in brachiopod shells: Calibrating a potential palaeoseasonality proxy: Chemical Geology, v. 397, p. 106–117, doi: 10.1016/J.CHEMGEO.2015.01.009.

Cai, J., Wu, W., and Liu, R., 2014, An overview of distributed activation energy model and its application in the pyrolysis of lignocellulosic biomass: Renewable and Sustainable Energy Reviews, v. 36, p. 236–246, doi: 10.1016/j.rser.2014.04.052.

Came, R.E., Eiler, J.M., Veizer, J., Azmy, K., Brand, U., and Weidman, C.R., 2007, Coupling of surface temperatures and atmospheric CO_2 concentrations during the Palaeozoic era: Nature, v. 449, p. 198–201, doi: 10.1038/nature06085.

Coogan, L.A., Daëron, M., and Gillis, K.M., 2019, Seafloor weathering and the oxygen isotope ratio in seawater: Insight from whole-rock $\delta^{18}O$ and carbonate $\delta^{18}O$ and Δ_{47} from the Troodos ophiolite: Earth and Planetary Science Letters, v. 508, p. 41–50, doi: 10.1016/j.epsl.2018.12.014.

Dale, A., John, C.M., Mozley, P.S., Smalley, P.C., and Muggeridge, A.H., 2014, Time-capsule concretions: Unlocking burial diagenetic processes in the Mancos Shale using carbonate clumped isotopes: Earth and Planetary Science Letters, v. 394, p. 30–37, doi: 10.1016/j.epsl.2014.03.004.

De Deckker, P., 2016, The Indo-Pacific Warm Pool: critical to world oceanography and world climate: Geoscience Letters, v. 3, doi: 10.1186/s40562-016-0054-3.

Defliese, W.F., and Lohmann, K.C., 2015, Non-linear mixing effects on mass-47 CO_2 clumped isotope thermometry: Patterns and implications: Rapid Communications in Mass Spectrometry, v. 29, p. 901–909, doi: 10.1002/rcm.7175.

Degens, E.T., and Epstein, S., 1962, Relationship Between $^{18}O/^{16}O$ Ratios in Coexisting Carbonates, Cherts, and Diatomites: GEOLOGICAL NOTES:, http://archives.datapages.com/data/bulletns/1961-64/images/pg/00460004/0500/05340.pdf (accessed January 2019).

Dennis, K.J., Affek, H.P., Passey, B.H., Schrag, D.P., and Eiler, J.M., 2011, Defining an absolute reference frame for "clumped" isotope studies of CO_2: Geochimica et Cosmochimica Acta, v. 75, p. 7117–7131, doi: 10.1016/j.gca.2011.09.025.

Eiler, J.M., 2007, "Clumped-isotope" geochemistry-The study of naturally-occurring, multiply-substituted isotopologues: Earth and Planetary Science Letters, v. 262, p. 309–327, doi: 10.1016/j.epsl.2007.08.020.

Eiler, J.M., 2011, Paleoclimate reconstruction using carbonate clumped isotope thermometry: Quaternary Science Reviews, v. 30, p. 3575–3588, doi: 10.1016/j.quascirev.2011.09.001.

Elrick, M., Reardon, D., Labor, W., Martin, J., Desrochers, A., and Pope, M., 2013, Orbital-scale climate change and glacioeustasy during the early late ordovician (pre-Hirnantian) determined from $\delta^{18}O$ values in marine apatite: Geology, v. 41, p. 775–778, doi: 10.1130/G34363.1.

Epstein, B.S., Buchsbaum, R., Lowenstam, H.A., and Urey, H.C., 1953, Revised carbonate-water isotopc temperature scale: v. 64, p. 1315–1326, doi: https://doi.org/10.1130/0016-7606(1953)64[1315:RCITS]2.0.CO;2.

Epstein, A.G., Epstein, J.B., and Harris, L.D., 1977, Conodont Color Alteration - an Index to Organic Metamorphism:, doi: 10.1130/0016-7606(1987)99<471:CCATAA>2.0.CO;2.

Ettensohn, F.R., Kasl, J.M., and Stewart, A.K., 2004, Structural inversion and origin of a Late Ordovician (Trenton) carbonate buildup: evidence from the Tanglewood and Devils Hollow members, Lexington Limestone, central Kentucky (USA): Palaeogeography, Palaeoclimatology, Palaeoecology, v. 210, p. 249–266, doi: 10.1016/J.PALAEO.2004.02.040.

Finnegan, S., Bergmann, K., Eiler, J.M., Jones, D.S., Fike, D.A., Eisenman, I., Hughes, N.C., Tripati, A.K., and Fischer, W.W., 2011, The magnitude and duration of late Ordovician-early Silurian glaciation: Science, v. 331, p. 903–906, doi: 10.1126/science.1200803.

Flake, R., 2011, Circulation of North American Epicontinental Seas during the Carboniferous using Stable Isotope and Trace Element Analyses of Brachiopod Shells: Texas A&M University, 86 p., https://core.ac.uk/download/pdf/9069043.pdf (accessed January 2019).

Forster, A., Schouten, S., Moriya, K., Wilson, P.A., and Damsté, J.S.S., 2007, Tropical warming and intermittent cooling during the Cenomanian/Turonian oceanic anoxic event 2: Sea surface temperature records from the equatorial Atlantic: Paleoceanography, v. 22, p. 1–14, doi: 10.1029/2006PA001349.

Frakes, L.A., Francis, J.E., and Syktus, J.I., 2005, Climate modes of the Phanerozoic: Cambridge University Press.

Frieling, J., Gebhardt, H., Huber, M., Adekeye, O.A., Akande, S.O., Reichart, G.J., Middelburg, J.J., Schouten, S., and Sluijs, A., 2017, Extreme warmth and heat-stressed plankton in the tropics during the Paleocene-Eocene Thermal Maximum: Science Advances, v. 3, doi: 10.1126/sciadv.1600891.

Galili, N., Shemesh, A., Yam, R., Brailovsky, I., Sela-Adler, M., Schuster, E.M., Collom, C., Bekker, A., Planavsky, N., Macdonald, F.A., Préat, A., Rudmin, M., Trela, W., Sturesson, U., et al., 2019, The geologic history of seawater oxygen isotopes from marine iron oxides.: Science (New York, N.Y.), v. 365, p. 469–473, doi: 10.1126/science.aaw9247.

Ghosh, P., Adkins, J., Affek, H., Balta, B., Guo, W., Schauble, E.A., Schrag, D., and Eiler, J.M., 2006, ^{13}C-^{18}O bonds in carbonate minerals: A new kind of paleothermometer: Geochimica et Cosmochimica Acta, v. 70, p. 1439–1456, doi: 10.1016/j.gca.2005.11.014.

Given, R.K., and Lohmann, K.C., 1985, Derivation of the original isotopic composition of Permian marine cements.: Journal of Sedimentary Petrology, v. 55, p. 430–439, doi: 10.1306/212F86F2-2B24-11D7-8648000102C1865D.

Grauel, A.-L., Schmid, T.W., Hu, B., Bergami, C., Capotondi, L., Zhou, L., and Bernasconi, S.M., 2013, Calibration and application of the 'clumped isotope' thermometer to foraminifera for high-resolution climate reconstructions: Geochimica et Cosmochimica Acta, v. 108, p. 125–140, doi: 10.1016/J.GCA.2012.12.049.

Grossman, E.L., 2012a, Applying Oxygen Isotope Paleothermometry in Deep Time: The Paleontological Society Papers, v. 18, p. 39–68, doi: 10.1017/s1089332600002540.

Grossman, E.L., 2012b, Oxygen Isotope Stratigraphy: The Geologic Time Scale 2012, v.

1–2, p. 181–206, doi: 10.1016/B978-0-444-59425-9.00010-X.

Grossman, E.L., Mii, H.-S., Zhang, C., and Yancey, T.E., 1996, Chemical variation in Pennsylvanian brachiopod shells - Diagenetic, taxonomic, microstructral, and seasonal effects: Journal of Sedimentary Research, v. 66, p. 1011–1022.

Harris, A.G., Harris, L.D., and Epstein, J.B., 1978, Oil and gas data from Paleozoic rocks in the Appalachian Basin; maps for assessing hydrocarbon potential and thermal maturity (conodont color alteration isograds and overburden isopachs).:

Hays, P.D., and Grossman, E.L., 1991, Oxygen isotopes in meteoric calcite cements as indicators of continental paleoclimate: Geology, v. 19, p. 441, doi: 10.1130/0091-7613(1991)019<0441:OIIMCC>2.3.CO;2.

Hemingway, J.D., and Henkes, G.A., 2020, A distributed activation energy model for clumped isotope bond reordering in carbonates:

Henkes, G.A., Passey, B.H., Grossman, E.L., Shenton, B.J., Pérez-Huerta, A., and Yancey, T.E., 2014, Temperature limits for preservation of primary calcite clumped isotope paleotemperatures: Geochimica et Cosmochimica Acta, v. 139, p. 362–382, doi: 10.1016/j.gca.2014.04.040.

Henkes, G.A., Passey, B.H., Grossman, E.L., Shenton, B.J., Yancey, T.E., and Pérez-Huerta, A., 2018, Temperature evolution and the oxygen isotope composition of Phanerozoic oceans from carbonate clumped isotope thermometry: Earth and Planetary Science Letters, v. 490, p. 40–50, doi: 10.1016/j.epsl.2018.02.001.

Herrmann, A.D., Macleod, K.G., and Leslie, S.A., 2010, Did a Volcanic Mega-Eruption Cause Global Cooling During the Late Ordovician ? Palaios, v. 25, p. 831–836, doi: 10.2110/palo.2010.p10-069r.

Hodel, F., Macouin, M., Trindade, R.I.F., Triantafyllou, A., Ganne, J., Chavagnac, V., Berger, J., Rospabé, M., Destrigneville, C., Carlut, J., Ennih, N., and Agrinier, P., 2018, Fossil black smoker yields oxygen isotopic composition of Neoproterozoic seawater: Nature Communications, v. 9, p. 1453, doi: 10.1038/s41467-018-03890-w.

Huntington, K.W., Budd, D.A., Wernicke, B.P., and Eiler, J.M., 2011, Use of Clumped-Isotope Thermometry To Constrain the Crystallization Temperature of Diagenetic Calcite: Journal of Sedimentary Research, v. 81, p. 656–669, doi: 10.2110/jsr.2011.51.

Huntington, K.W., and Lechler, A.R., 2015, Carbonate clumped isotope thermometry in continental tectonics: Tectonophysics, v. 647, p. 1–20,

doi:10.1016/j.tecto.2015.02.019.

Jaffrés, J.B.D., Shields, G.A., and Wallmann, K., 2007, The oxygen isotope evolution of seawater: A critical review of a long-standing controversy and an improved geological water cycle model for the past 3.4 billion years: Earth-Science Reviews, v. 83, p. 83–122, doi: 10.1016/J.EARSCIREV.2007.04.002.

Jautzy, J.J., Savard, M.M., Dhillon, R.S., and Bernasconi, S.M., 2020, Clumped isotope temperature calibration for calcite: Bridging theory and experimentation: Geochemical Perspectives Letters, p. 36–41, doi: 10.7185/geochemlet.2021.

Joachimski, M.M., Breisig, S., Buggisch, W., Talent, J.A., Mawson, R., Gereke, M., Morrow, J.R., Day, J., and Weddige, K., 2009, Devonian climate and reef evolution: Insights from oxygen isotopes in apatite: Earth and Planetary Science Letters, v. 284, p. 599–609, doi: 10.1016/J.EPSL.2009.05.028.

Joachimski, M.M., van Geldern, R., Breisig, S., Buggisch, W., and Day, J., 2004, Oxygen isotope evolution of biogenic calcite and apatite during the Middle and Late Devonian: International Journal of Earth Sciences, v. 93, p. 542–553, doi: 10.1007/s00531-004-0405-8.

John, C.M., and Bowen, D., 2016, Community software for challenging isotope analysis: First applications of 'Easotope' to clumped isotopes: Rapid Communications in Mass Spectrometry, v. 30, p. 2285–2300, doi: 10.1002/rcm.7720.

Judd, E., Bhattacharya, T., and Ivany, L., 2020, A dynamical framework for interpreting ancient sea surface temperatures: Geophysical Research Letters, doi: 10.1029/2020GL089044.

Kele, S., Breitenbach, S.F.M., Capezzuoli, E., Meckler, A.N., Ziegler, M., Millan, I.M., Kluge, T., Deák, J., Hanselmann, K., John, C.M., Yan, H., Liu, Z., and Bernasconi, S.M., 2015, Temperature dependence of oxygen- and clumped isotope fractionation in carbonates: A study of travertines and tufas in the 6–95 °C temperature range: Geochimica et Cosmochimica Acta, v. 168, p. 172–192, doi: 10.1016/J.GCA.2015.06.032.

Kendall, A.C., 1985, Radiaxial fibrous calcite: a reappraisal (Western Australia).: Carbonate cements, p. 59–77.

Kim, J.C., and Lee, Y. Il, 1996, Marine diagenesis of Lower Ordovician carbonate sediments (Dumugol Formation), Korea: Cementation in a calcite sea: Sedimentary Geology, v. 105, p. 241–257, doi: 10.1016/0037-0738(95)00141-7.

Kim, S.-T., Mucci, A., and Taylor, B.E., 2007, Phosphoric acid fractionation factors for

calcite and aragonite between 25 and 75 °C: Revisited: Chemical Geology, v. 246, p. 135–146, doi: 10.1016/J.CHEMGEO.2007.08.005.

Kim, S.-T., and O'Neil, J.R., 1997, Equilibrium and nonequilibrium oxygen isotope effects in synthetic carbonates: Geochimica et Cosmochimica Acta, v. 61, p. 3461–3475, doi: 10.1016/S0016-7037(97)00169-5.

Kolata, D.R., Huff, W.D., and Bergström, S.M., 2001, The Ordovician Sebree Trough: An oceanic passage to the Midcontinent United States: Geological Society of America Bulletin, v. 113, p. 1067–1078, doi: 10.1130/0016-7606(2001)113<1067:TOSTAO>2.0.CO;2.

Kronenberg, A.K., Yund, R.A., and Giletti, B.J., 1984, Carbon and oxygen diffusion in calcite: Effects of Mn content and PH_2O: Physics and Chemistry of Minerals, v. 11, p. 101–112, doi: 10.1007/BF00309248.

Lécuyer, C., Grandjean, P., and Martineau, F., 1995, Seawater-sediment-basalt interactions: stable isotope (H, O) and elemental fluxes within the Ordovician volcano-sedimentary sequence of Erquy (Brittany, France): Contributions to Mineralogy and Petrology, v. 120, p. 249–264, doi: 10.1007/BF00306506.

Lee, X., and Wan, G., 2000, No vital effect on $\delta^{18}O$ and $\delta^{13}C$ values of fossil brachiopod shells, Middle Devonian of China: Geochimica et Cosmochimica Acta, v. 64, p. 2649–2664, doi: 10.1016/S0016-7037(99)00438-X.

Lohmann, K.C., and Walker, J.C.G., 1989, The $\delta^{18}0$ Record of Phanerozoic Aboitic Marine Calcite Cements: Geophysical Research Letters, v. 16, p. 319–322.

Marshall, J.D., and Middleton, P.D., 1990, Changes in marine isotopic composition and the late Ordovician glaciation: Journal of the Geological Society, v. 147, p. 1–4, doi: 10.1144/gsjgs.147.1.0001.

Meckler, A.N., Ziegler, M., Millán, M.I., Breitenbach, S.F.M., and Bernasconi, S.M., 2014, Long-term performance of the Kiel carbonate device with a new correction scheme for clumped isotope measurements: Rapid Communications in Mass Spectrometry, v. 28, p. 1705–1715, doi: 10.1002/rcm.6949.

Meinicke, N., Ho, S.L., Hannisdal, B., Nürnberg, D., Tripati, A., Schiebel, R., and Meckler, A.N., 2020, A robust calibration of the clumped isotopes to temperature relationship for foraminifers: Geochimica et Cosmochimica Acta, v. 270, p. 160–183, doi: 10.1016/j.gca.2019.11.022.

Melim, L.A., Swart, P.K., and Maliva, R.G., 1995, Meteoric-like fabrics forming in marine waters: implications for the use of petrography to identify diagenetic

environments: Geology, v. 23, p. 755–758, doi: 10.1130/0091-7613(1995)023<0755:MLFFIM>2.3.CO;2.

Muehlenbachs, K., 1998, The oxygen isotopic composition of the oceans, sediments and the seafloor: Chemical Geology, v. 145, p. 263–273, https://ac-els-cdn-com.lib-ezproxy.tamu.edu:9443/S0009254197001472/1-s2.0-S0009254197001472-main.pdf?_tid=49aef98c-b52b-46cf-affa-eff226a546a7&acdnat=1539058685_1485571b5f388d6298d15ca7acbaa3c2 (accessed October 2018).

Muehlenbachs, K., Furnes, H., Fonneland, H.C., and Hellevang, B., 2003, Ophiolites as faithful records of the oxygen isotope ratio of ancient seawater: the Solund-Stavfjord Ophiolite Complex as a Late Ordovician example: Geological Society, London, Special Publications, v. 218, p. 401–414, doi: 10.1144/GSL.SP.2003.218.01.20.

Passey, B.H., and Henkes, G.A., 2012, Carbonate clumped isotope bond reordering and geospeedometry: Earth and Planetary Science Letters, v. 351–352, p. 223–236, doi: 10.1016/j.epsl.2012.07.021.

Patzkowsky, M.E., and Holland, S.M., 1993, Biotic response to a Middle Ordovician paleoceanographic event in eastern North America: Geology, v. 21, p. 619, doi: 10.1130/0091-7613(1993)021<0619:BRTAMO>2.3.CO;2.

Peral, M., Daëron, M., Blamart, D., Bassinot, F., Dewilde, F., Smialkowski, N., Isguder, G., Bonnin, J., Jorissen, F., Kissel, C., Michel, E., Vázquez Riveiros, N., and Waelbroeck, C., 2018, Updated calibration of the clumped isotope thermometer in planktonic and benthic foraminifera: Geochimica et Cosmochimica Acta, v. 239, p. 1–16, doi: 10.1016/j.gca.2018.07.016.

Petersen, S. V., Defliese, W.F., Saenger, C., Daëron, M., Huntington, K.W., John, C.M., Kelson, J.R., Bernasconi, S.M., Colman, A.S., Kluge, T., Olack, G.A., Schauer, A.J., Bajnai, D., Bonifacie, M., et al., 2019, Effects of Improved ^{17}O Correction on Interlaboratory Agreement in Clumped Isotope Calibrations, Estimates of Mineral-Specific Offsets, and Temperature Dependence of Acid Digestion Fractionation: Geochemistry, Geophysics, Geosystems, v. 20, p. 3495–3519, doi: 10.1029/2018GC008127.

Please, C.P., McGuinness, M.J., and McElwain, D.L.S., 2003, Approximations to the distributed activation energy model for the pyrolysis of coal: Combustion and Flame, v. 133, p. 107–117, doi: 10.1016/S0010-2180(02)00554-0.

Pope, M.C., Holland, S.M., and Patzkowsky, M.E., 2012, The Cincinnati Arch: A Stationary Peripheral Bulge during the Late Ordovician: Perspectives in Carbonate Geology, v. 2812, p. 255–275, doi: 10.1002/9781444312065.ch16.

Pope, M.C., and Read, J.F., 1997, High-Resolution Stratigraphy of the Lexington Limestone (Late Middle Ordovician), Kentucky, U.S.a.: a Cool-Water Carbonate-Clastic Ramp in a Tectonically Active Foreland Basin: Cool-Water Carbonates, p. 411–429, doi: 10.2110/pec.97.56.0411.

Pope, M., and Read, J.F., 1998, Ordovician metre-scale cycles: implications for climate and eustatic fluctuations in the central Appalachians during a global greenhouse, non-glacial to glacial transition: Palaeogeography, Palaeoclimatology, Palaeoecology, v. 138, p. 27–42, doi: 10.1016/S0031-0182(97)00130-2.

Popp, B.N., Anderson, T.F., and Sandberg, P.A., 1986, Brachiopods as indicator of original isotopic composition in some Paleozoic limestones: Bulletin of the Geological Society of America, v. 97, p. 1262–1269, doi: 10.1130/0016-7606(1986)97<1262.

Qing, H., and Veizer, J., 1994, Oxygen and carbon isotopic composition of Ordovician brachiopods: Implications for coeval seawater: Geochimica et Cosmochimica Acta, v. 58, p. 4429–4442, doi: 10.1016/0016-7037(94)90345-X.

Quinton, P.C., Law, S., Macleod, K.G., Herrmann, A.D., Haynes, J.T., and Leslie, S.A., 2018, Testing the early Late Ordovician cool-water hypothesis with oxygen isotopes from conodont apatite: Geological Magazine, v. 155, p. 1727–1741, doi: 10.1017/S0016756817000589.

Quinton, P.C., and MacLeod, K.G., 2014, Oxygen isotopes from conodont apatite of the midcontinent, US: Implications for Late Ordovician climate evolution: Palaeogeography, Palaeoclimatology, Palaeoecology, v. 404, p. 57–66, doi: 10.1016/J.PALAEO.2014.03.036.

Rasmussen, C.M.Ø., Ullmann, C. V., Jakobsen, K.G., Lindskog, A., Hansen, J., Hansen, T., Eriksson, M.E., Dronov, A., Frei, R., Korte, C., Nielsen, A.T., and Harper, D.A.T., 2016, Onset of main Phanerozoic marine radiation sparked by emerging Mid Ordovician icehouse: Scientific Reports, v. 6, p. 1–9, doi: 10.1038/srep18884.

Ross, S.M., 2003, Peirce's criterion for the elimination of suspect experimental data: Journal of Engineering Technology, v. 20, p. 38–41.

Ryder, R.T., 1987, Oil and gas resources of the Cincinnati Arch, Ohio, Indiana, Kentucky, and Tennessee. U.S. Geological Survey Open-File Report 87-450Y:, doi: https://doi.org/10.3133/ofr87450Y.

Saller, A.H., and Moore, C.H., 1991, Geochemistry of meteoric calcite cements in some Pleistocene limestones: Sedimentology, v. 38, p. 601–621, doi: 10.1111/j.1365-3091.1991.tb01011.x.

Schmid, T.W., and Bernasconi, S.M., 2010, An automated method for “clumped-isotope” measurements on small carbonate samples: Rapid Communications in Mass Spectrometry, v. 24, p. 1955–1963, doi: 10.1002/rcm.4598.

Scotese, C.R., 2016, PALEOMAP PaleoAtlas for GPlates and the PaleoData Plotter Program: Updated at: https://www. earthbyte. org/paleomap-paleoatlas-for-gplates/, accessed, v. 1.

Shenton, B.J., Grossman, E.L., Passey, B.H., Henkes, G.A., Becker, T.P., Laya, J.C., Perez-Huerta, A., Becker, S.P., and Lawson, M., 2015, Clumped isotope thermometry in deeply buried sedimentary carbonates: The effects of bond reordering and recrystallization: Bulletin of the Geological Society of America, v. 127, p. 1036–1051, doi: 10.1130/B31169.1.

Shields, G.A., Carden, G.A.F., Veizer, J., Meidla, T., Rong, J.Y., and Li, R.Y., 2003, Sr, C, and O isotope geochemistry of Ordovician brachiopods: A major isotopic event around the Middle-Late Ordovician transition: Geochimica et Cosmochimica Acta, v. 67, p. 2005–2025, doi: 10.1016/S0016-7037(02)01116-X.

Sluijs, A., Bijl, P.K., Schouten, S., Röhl, U., Reichart, G.J., and Brinkhuis, H., 2011, Southern ocean warming, sea level and hydrological change during the Paleocene-Eocene thermal maximum: Climate of the Past, v. 7, p. 47–61, doi: 10.5194/cp-7-47-2011.

Stolper, D.A., and Eiler, J.M., 2015, The kinetics of solid-state isotope-exchange reactions for clumped isotopes: A study of inorganic calcites and apatites from natural and experimental samples: American Journal of Science, v. 315, p. 363–411, doi: 10.2475/05.2015.01.

Stolper, D.A., Eiler, J.M., and Higgins, J.A., 2018, Modeling the effects of diagenesis on carbonate clumped-isotope values in deep- and shallow-water settings: Geochimica et Cosmochimica Acta, v. 227, p. 264–291, doi: 10.1016/j.gca.2018.01.037.

Tobin, K.J., Steinhauff, D.M., and Walker, K.R., 1999, Ordovician meteoric carbon and oxygen isotopic values: Implications for the latitudinal variations of ancient stable isotopic values: Palaeogeography, Palaeoclimatology, Palaeoecology, v. 150, p. 331–342, doi: 10.1016/S0031-0182(98)00221-1.

Tobin, K.J., and Walker, K.R., 1996, Ordovician low- to intermediate-Mg calcite marine cements from Sweden: Marine alteration and implications for oxygen isotopes in Ordovician seawater: Sedimentology, v. 43, p. 719–735, doi: 10.1111/j.1365-3091.1996.tb02022.x.

Tobin, K.J., and Walker, K.R., 1997, Ordovician oxygen isotopes and paleotemperatures: Palaeogeography, Palaeoclimatology, Palaeoecology, v. 129, p. 269–290, doi: 10.1016/S0031-0182(96)00109-5.

Trotter, J.A., Williams, I.S., Barnes, C.R., Lécuyer, C., and Nicoll, R.S., 2008, Did cooling oceans trigger Ordovician biodiversification? Evidence from conodont thermometry: Science, v. 321, p. 550–554, doi: 10.1126/science.1155814.

Veizer, J., Ala, D., Azmy, K., Bruckschen, P., Buhl, D., Bruhn, F., Garden, G.A.F., Diener, A., Ebneth, S., Godderis, Y., Jasper, T., Korte, C., Pawellek, F., Podlaha, O.G., et al., 1999, $^{87}Sr/^{86}Sr$, $\delta^{13}C$ and $\delta^{18}O$ evolution of Phanerozoic seawater: Chemical Geology, v. 161, p. 59–88, doi: 10.1016/S0009-2541(99)00081-9.

Veizer, J., and Prokoph, A., 2015, Temperatures and oxygen isotopic composition of Phanerozoic oceans: Earth-Science Reviews, v. 146, p. 92–104, doi: 10.1016/j.earscirev.2015.03.008.

Wadleigh, M.A., and Veizer, J., 1992, $^{18}O/^{16}O$ and $^{13}C/^{12}C$ in lower Paleozoic articulate brachiopods: Implications for the isotopic composition of seawater: Geochimica et Cosmochimica Acta, v. 56, p. 431–443, doi: 10.1016/0016-7037(92)90143-7.

Wallmann, K., 2001, The geological water cycle and the evolution of marine $\delta^{18}O$ values: Geochimica et Cosmochimica Acta, v. 65, p. 2469–2485, doi: 10.1016/S0016-7037(01)00603-2.

Wefer, G., and Berger, W.H., 1991, Isotope paleontology: growth and composition of extant calcareous species: Marine Geology, v. 100, p. 207–248, doi: 10.1016/0025-3227(91)90234-U.

Wilkinson, B.H., Janecke, S.U., and Brett, C.E., 1982, Low-magnesium calcite marine cement in Middle Ordovician hardgrounds from Kirkfield, Ontario (Canada).: Journal of sedimentary petrology, v. 52, p. 47–57.

Wilkinson, B.H., Smith, A.L., and Lohmann, K.C., 1985, Sparry calcite marine cement in Upper Jurassic limestones of southeastern Wyoming (USA, Oxfordian).: Carbonate cements, p. 169–184.

Wilson, M.A., and Palmer, T.J., 1992, Hardgrounds and hardground faunas: University of Wales, Aberystwyth, v. 9, 131 p.

APPENDIX 1

Table 2. Trace element data and cathodoluminescence for measured brachiopods

Sample	Ca (ppm)	Fe (ppm)	Mg (ppm)	Mn (ppm)	Na (ppm)	Sr (ppm)	CL rating
65983	217532	165	1338	112	487	384	CL
OKP-1	200547	228	1697	64	569	1777	SL
OKH-1	174036	139	1472	64	431	311	NL/SL
66378	165288	47	1104	20	523	292	NL
27542	193556	215	1220	227	459	327	CL
68984	211627	64	1049	26	711	716	NL
CCSP-1	164992	117	929	20	474	375	NL
CCSP-2	189695	166	1260	124	475	305	SL/CL
27638	170933	67	1140	40	560	562	NL
2142-1	195319	30	1261	10	616	508	NL
27724	170960	47	1082	78	585	790	NL
51149	154552	74	888	97	487	1513	NL
51000	159657	25	1100	22	492	350	NL/SL
63678	185110	50	1019	44	539	367	NL
69459	179122	193	1658	101	575	1191	NL
78682-2	178039	72	1198	9	538	714	NL
63696	187385	24	1182	69	562	314	NL
78700	185917	48	1662	11	621	513	NL
27909-1	179444	9	1064	7	599	284	NL
27921	208961	20	1282	26	656	436	NL
MCP-1	164350	55	1233	33	474	599	N/SL
MCP-5	199338	188	1511	156	643	442	NL
MCH-1	168433	237	1209	43	518	692	SL
MCH-3	191490	315	1150	208	459	139	CL
27969-1	218887	99	1721	114	659	594	NL/SL
68818	161767	41	999	7	523	349	NL
68980	170916	120	1335	125	455	212	NL/SL
68766	122119	27	920	10	427	188	NL/SL

Table 3. Age, formation, and location data for brachiopod shells from this study

Sample	Material	Taxon	Age (Ma)	Period	Global Stage	N. American Stage	Formation	Member	Lithology
65983	Brachiopod	*Hebertella*	443.5	Silurian	Rhuddanian	Alexandrian	Brassfield		Limestone
OKP-1	Brachiopod	*Vinlandostrophia*	446.5	Ordovician	Katian	Cincinnatian	Richmondian	Drakes	Limestone
OKH-1	Brachiopod	*Hebertella*	446.5	Ordovician	Katian	Cincinnatian	Richmondian	Drakes	Limestone
66378	Brachiopod	*Vinlandostrophia*	446.7	Ordovician	Katian	Cincinnatian	Richmondian	Whitewater	Limestone
27542	Brachiopod	*Hebertella*	446.7	Ordovician	Katian	Cincinnatian	Richmondian	Whitewater	Limestone
68984	Brachiopod	*Hebertella*	446.8	Ordovician	Katian	Cincinnatian	Richmondian	Whitewater	Limestone
CCSP-1	Brachiopod	*Hebertella*	446.9	Ordovician	Katian	Cincinnatian	Richmondian	Liberty	Limestone
CCSP-2	Brachiopod	*Vinlandostrophia*	446.9	Ordovician	Katian	Cincinnatian	Richmondian	Liberty	Limestone
27638	Brachiopod	*Vinlandostrophia*	447	Ordovician	Katian	Cincinnatian	Richmondian	Waynesville	Shale
2142-1	Brachiopod	*Vinlandostrophia*	447	Ordovician	Katian	Cincinnatian	Richmondian	Waynesville	Shale
27724	Brachiopod	*Hebertella*	447	Ordovician	Katian	Cincinnatian	Richmondian	Waynesville	Limestone
51149	Brachiopod	*Hebertella*	447.2	Ordovician	Katian	Cincinnatian	Richmondian	Waynesville	Shale
51000	Brachiopod	*Vinlandostrophia*	447.3	Ordovician	Katian	Cincinnatian	Richmondian	Arnheim	Shale
63678	Brachiopod	*Hebertella*	447.3	Ordovician	Katian	Cincinnatian	Richmondian	Arnheim	Shale
69459	Brachiopod	*Vinlandostrophia*	447.4	Ordovician	Katian	Cincinnatian	Richmondian	Arnheim	Shale
78682-2	Brachiopod	*Vinlandostrophia*	447.5	Ordovician	Katian	Cincinnatian	Maysvillian	Grant Lake	Limestone
63696	Brachiopod	*Hebertella*	447.6	Ordovician	Katian	Cincinnatian	Maysvillian	Grant Lake	Limestone
78700	Brachiopod	*Vinlandostrophia*	447.6	Ordovician	Katian	Cincinnatian	Maysvillian	Grant Lake	Limestone
27909-1	Brachiopod	*Vinlandostrophia*	447.7	Ordovician	Katian	Cincinnatian	Maysvillian	Grant Lake	Limestone
27921	Brachiopod	*Hebertella*	447.8	Ordovician	Katian	Cincinnatian	Maysvillian	Grant Lake	Limestone
MCP-1	Brachiopod	*Vinlandostrophia*	447.8	Ordovician	Katian	Cincinnatian	Maysvillian	Grant Lake	Limestone
MCP-5	Brachiopod	*Vinlandostrophia*	447.8	Ordovician	Katian	Cincinnatian	Maysvillian	Grant Lake	Limestone
MCH-1	Brachiopod	*Hebertella*	447.8	Ordovician	Katian	Cincinnatian	Maysvillian	Grant Lake	Limestone
MCH-3	Brachiopod	*Hebertella*	447.8	Ordovician	Katian	Cincinnatian	Maysvillian	Grant Lake	Limestone
27969-1	Brachiopod	*Vinlandostrophia*	447.8	Ordovician	Katian	Cincinnatian	Maysvillian	Grant Lake	Limestone
68818	Brachiopod	*Vinlandostrophia*	447.9	Ordovician	Katian	Cincinnatian	Maysvillian	Fairview	Limestone
68980	Brachiopod	*Hebertella*	448.5	Ordovician	Katian	Cincinnatian	Maysvillian	Fairview	Shale
68766	Brachiopod	*Vinlandostrophia*	449	Ordovician	Katian	Cincinnatian	Edenian	Kope	Shale

Table 3 Continued

Sample	Location	Locality	Latitude	Longitude	*Paleo-latitude	*Paleo-longitude
65983	Cincinnati Arch	Montgomery County, Ohio	39.769	-84.359	-23.8803	-55.6484
OKP-1	Cincinnati Arch	Owingsville, KY	38.12949	-83.75221	-26.0588	-57.7907
OKH-1	Cincinnati Arch	Owingsville, KY	38.12949	-83.75221	-26.0588	-57.7907
66378	Cincinnati Arch	Route 27, IN South of Richmond, IN	39.78745	-84.90181	-24.2261	-57.6272
27542	Cincinnati Arch	Branch Cedar Creek, Versailles, IN	39.0806	-85.2339	-24.6435	-58.3142
68984	Cincinnati Arch	Causeway Rd., Frankfort, OH	39.4019	-83.1856	-25.3242	-56.7369
CCSP-1	Cincinnati Arch	Caesar Creek Spillway	39.4791	-84.0572	-24.8924	-57.348
CCSP-2	Cincinnati Arch	Caesar Creek Spillway	39.4791	-84.0572	-24.8924	-57.348
27638	Cincinnati Arch	Big 4 R.R. cut Weisburg, IN	39.22271	-85.04886	-24.6659	-58.2486
2142-1	Cincinnati Arch	South Gate Hill cut, IN Route 1, Cedar Grove, IN	39.3390	-84.9524	-24.6169	-58.1064
27724	Cincinnati Arch	Big 4 R.R., Weisburg, IN	39.22271	-85.04886	-24.6659	-58.2486
51149	Cincinnati Arch	Weisburg, IN	39.22271	-85.04886	-24.6999	-58.3515
51000	Cincinnati Arch	Big 4 cut Maud, OH	39.34867	-84.39059	-24.9182	-57.8691
63678	Cincinnati Arch	Westwood, OH	39.16325	-84.60169	-24.9711	-58.1354
69459	Cincinnati Arch	Adams Co., Ohio	39.9352	-83.64736	-24.7943	-57.0312
78682-2	Cincinnati Arch	Maud, OH	39.34867	-84.39059	-24.953	-57.9726
63696	Cincinnati Arch	L&N R.R. cut Walton, KY	38.8848	-84.6088	-25.2426	-58.4794
78700	Cincinnati Arch	Blue Rock Rd. Herm Co.	39.23057	-84.62198	-24.9589	-58.2607
27909-1	Cincinnati Arch	L&N R.R. cut Walton, KY	38.8848	-84.6088	-25.2594	-58.5316
27921	Cincinnati Arch	L&N R.R. Cut, Walton, KY	38.8848	-84.6088	-25.2761	-58.5839
MCP-1	Cincinnati Arch	Maysville Big Cut	38.67655	-83.79633	-25.8198	-58.1562
MCP-5	Cincinnati Arch	Maysville Big Cut	38.67655	-83.79633	-25.8198	-58.1562
MCH-1	Cincinnati Arch	Maysville Big Cut	38.67655	-83.79633	-25.8198	-58.1562
MCH-3	Cincinnati Arch	Maysville Big Cut	38.67655	-83.79633	-25.8198	-58.1562
27969-1	Cincinnati Arch	Walton, KY	38.8848	-84.6088	-25.2761	-58.5839
68818	Cincinnati Arch	Cut west of Georgetown, OH	38.87543	-83.93021	-25.6148	-58.1723
68980	Cincinnati Arch	Marble Hill site, 10 miles west of Carrollton, KY	38.62747	-85.14889	-25.2597	-59.2316
68766	Cincinnati Arch	Marble Hill site, 10 miles west of Carrollton, KY	38.62747	-85.14889	-25.4172	-59.7564

*Paleo-latitude and longitude calculated using GPlates 2.0 and PALEOMAP PaleoAtlas. (Scotese, 2016)

APPENDIX 2

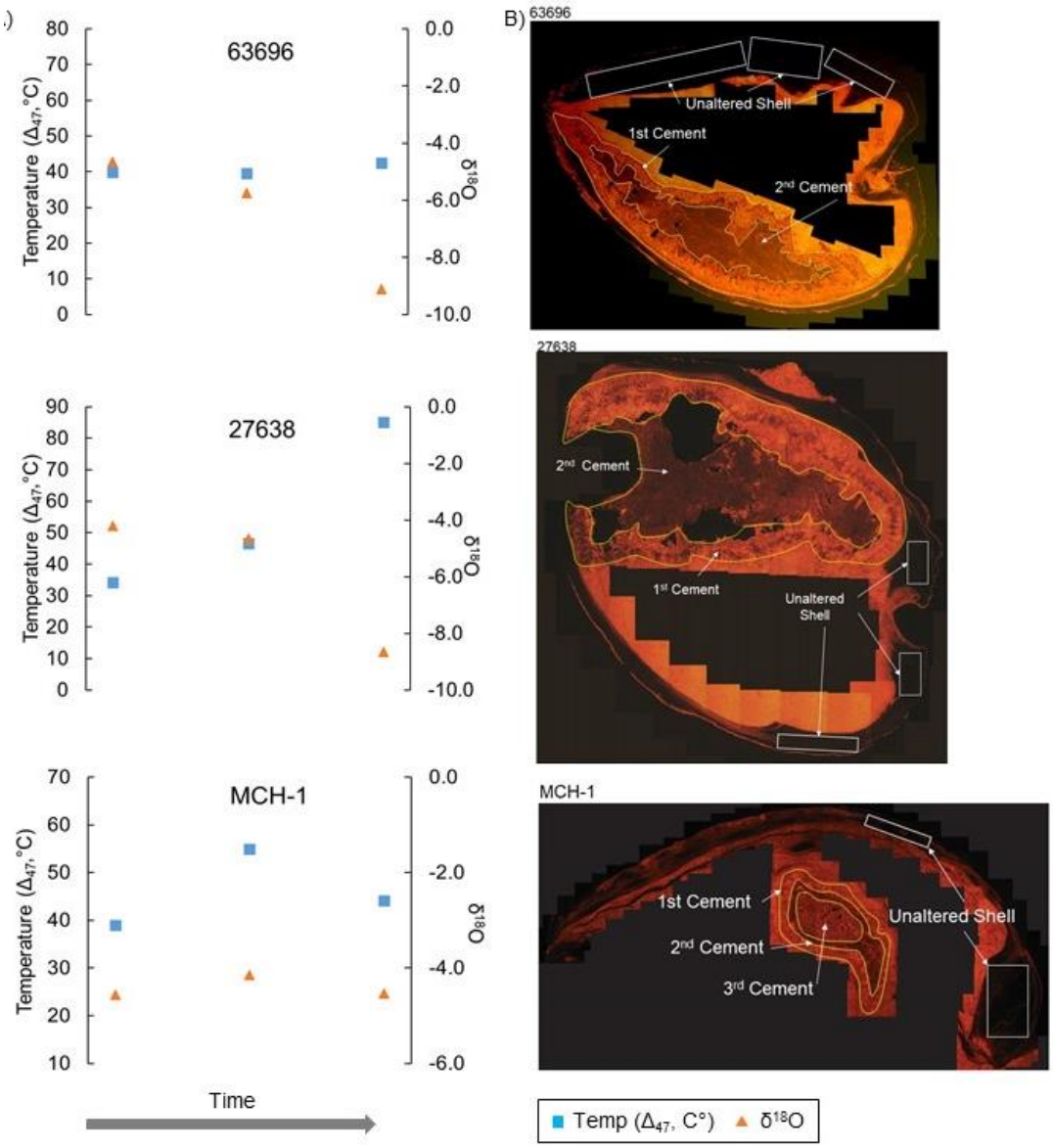

Figure 16. A) Δ_{47} temperatures, and $\delta^{18}O_{carb}$ of brachiopod shells (leftmost) and the internal multi-generational cements within the shell. Blue squares represent Δ_{47} temperatures. Orange triangles represent $\delta^{18}O_{carb}$. B) Cathodoluminescence images of brachiopod shells and internal multi-generational cements measured. The 2nd cement within Shell MCH-1 was not measured due to insufficient material. The graph shows data from the brachiopod shell, the 1st and 3rd generation of cement (bottom right).

CM #65983

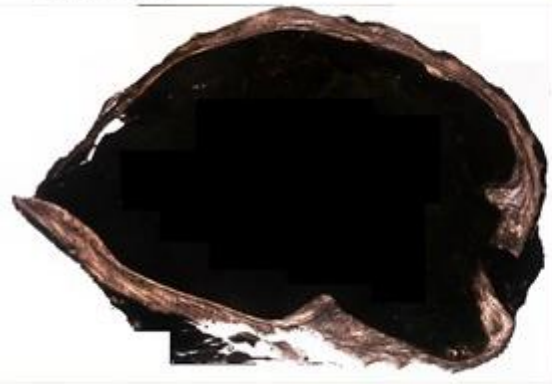

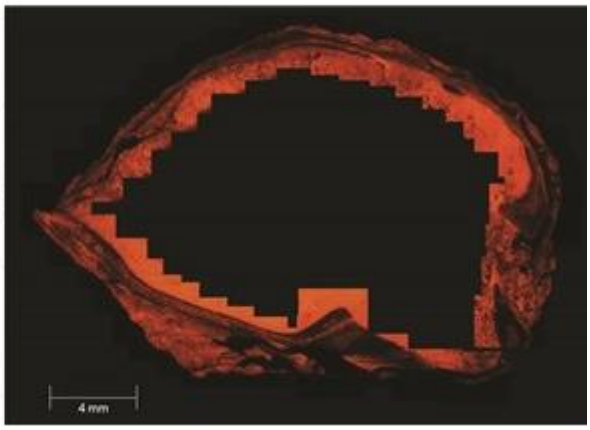

OKP-1

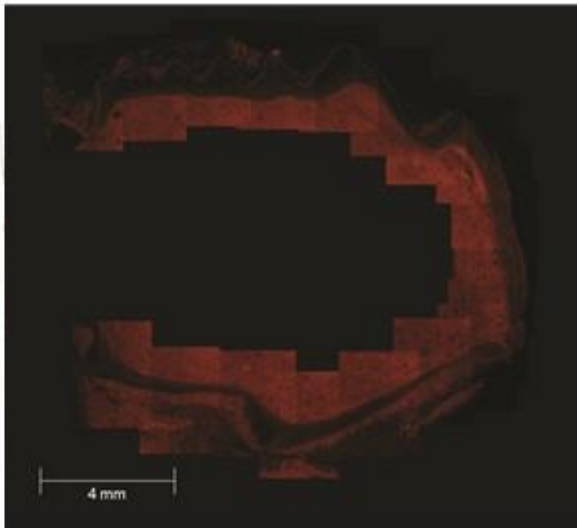

OKH-1

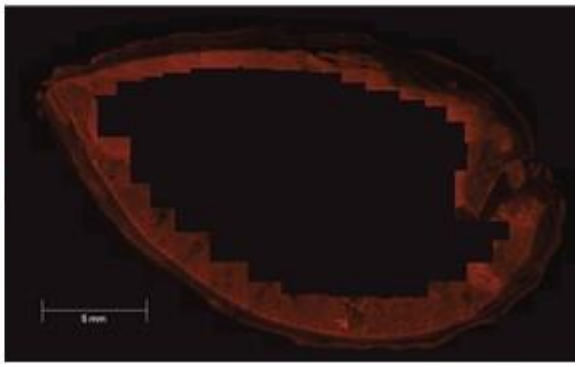

CM #66378

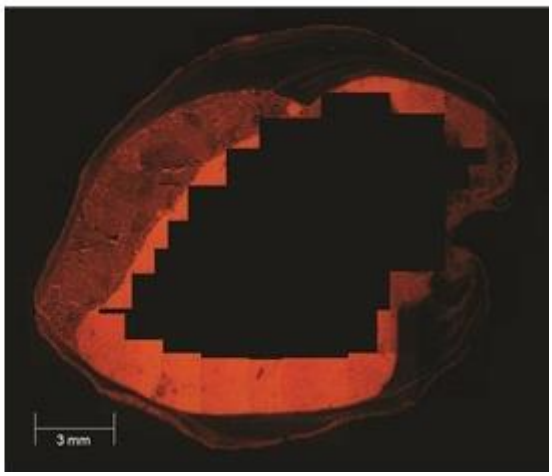

CM #27542

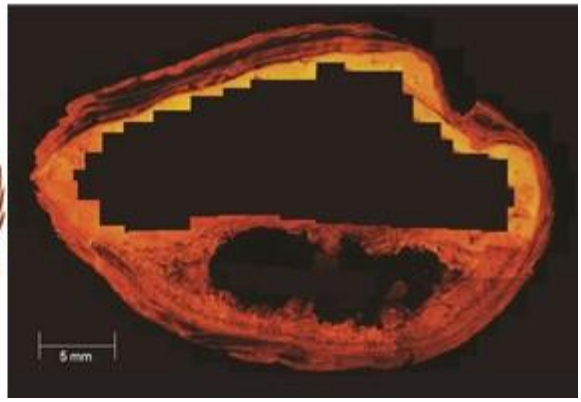

CM #68984

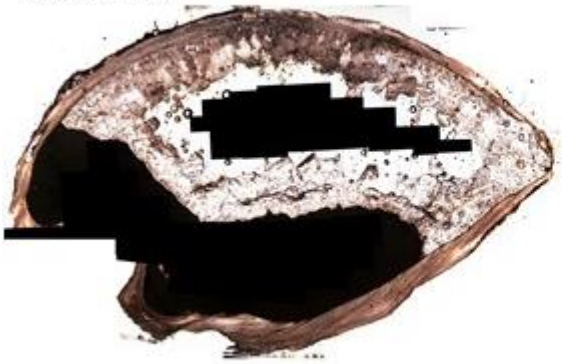

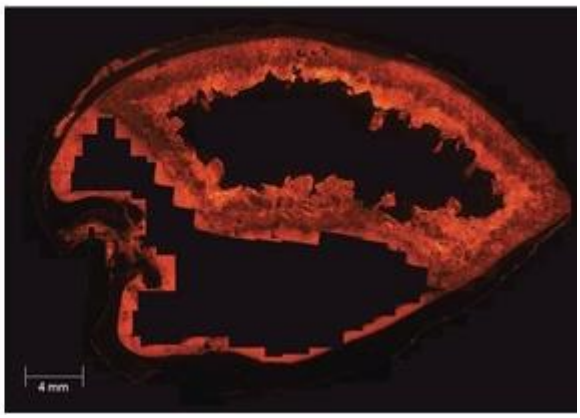

CCSP-1

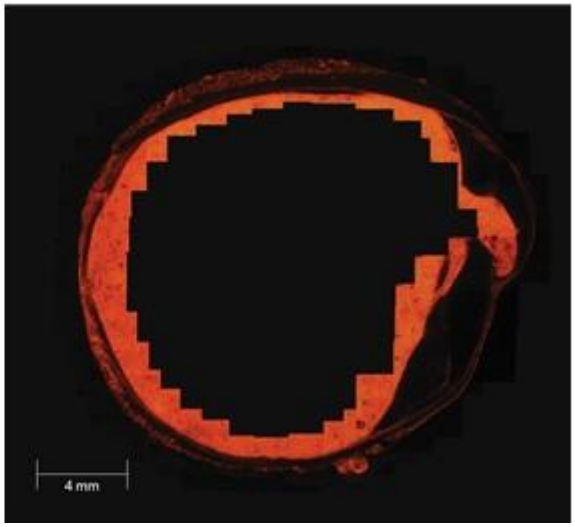

CCSP-2

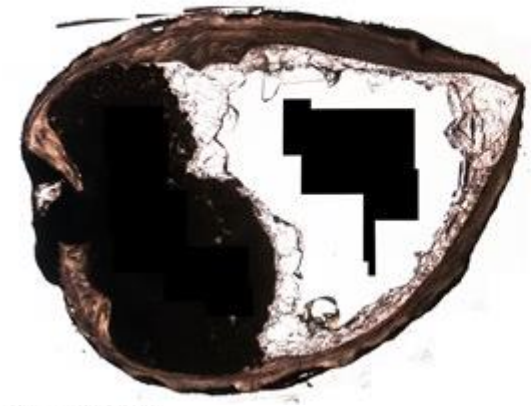

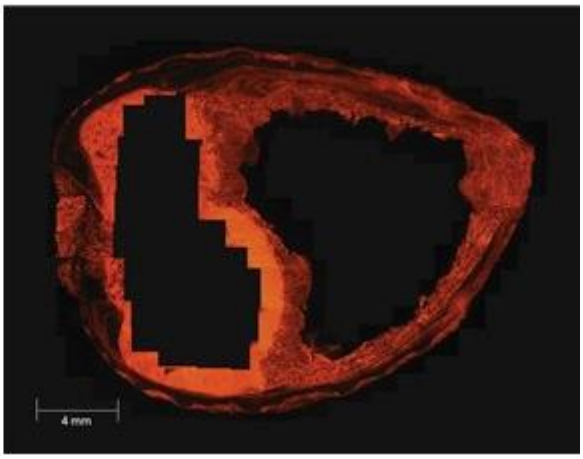

CM #27638

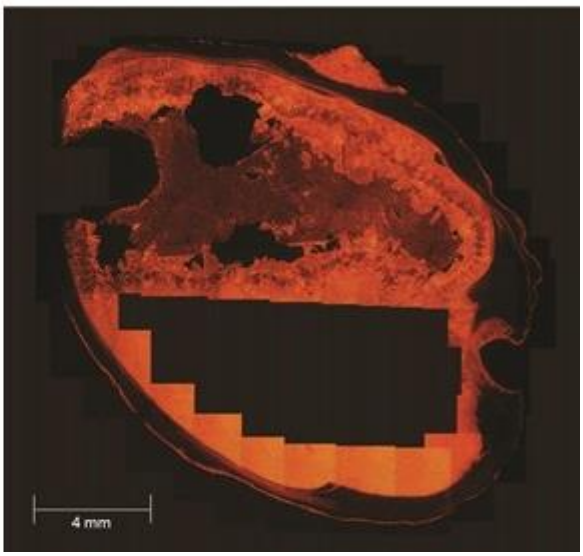

CM #2142

CM #27724

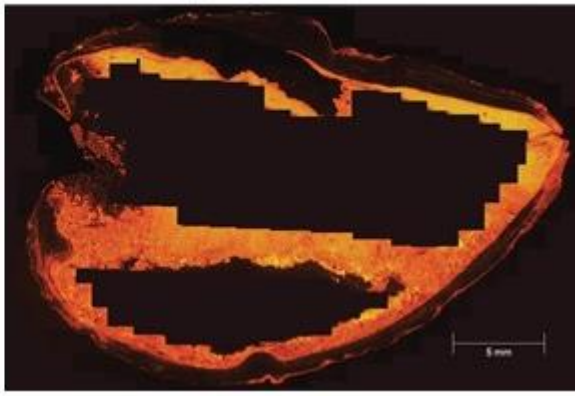

CM #51149

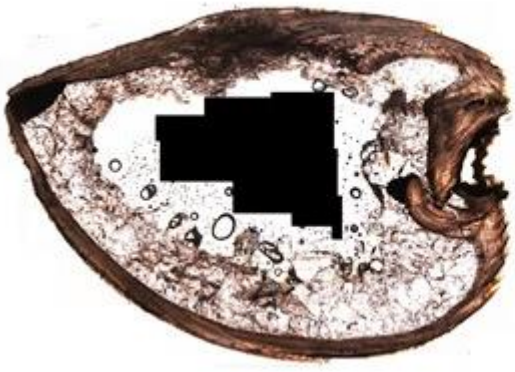

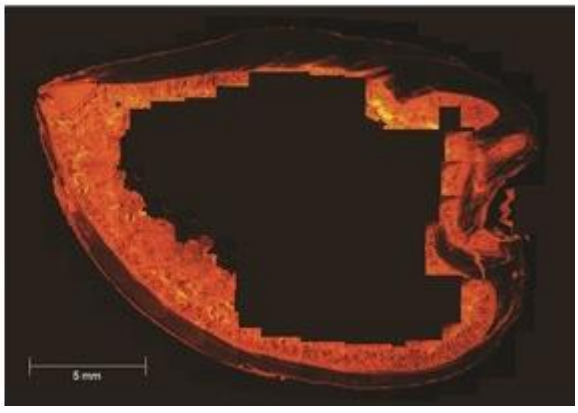

CM #51000

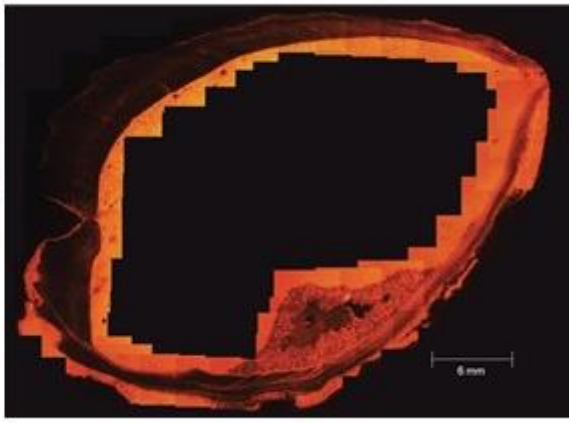

CM #63677

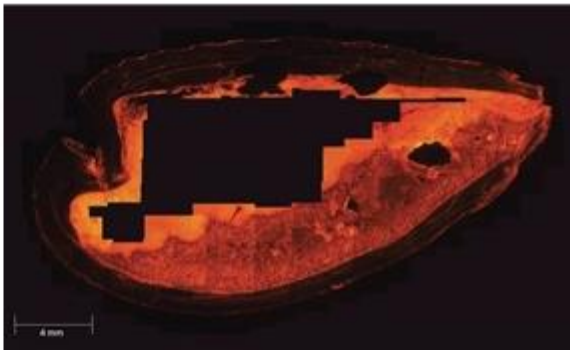

CM #69459

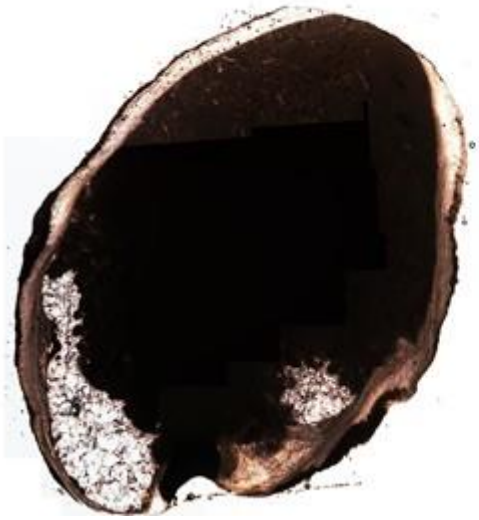

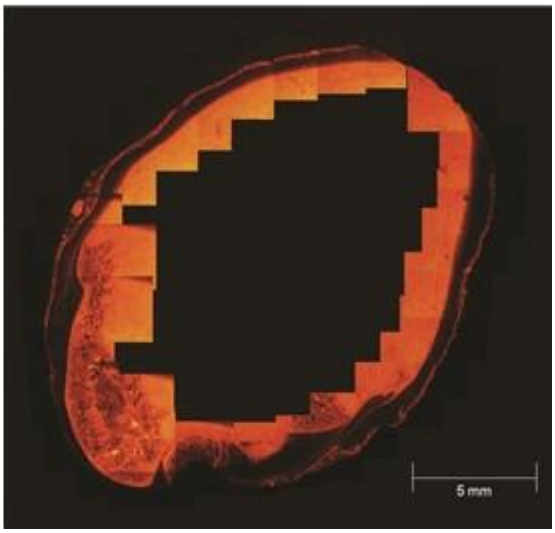

CM #63696

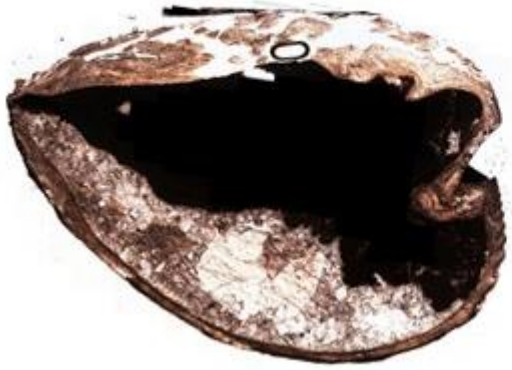

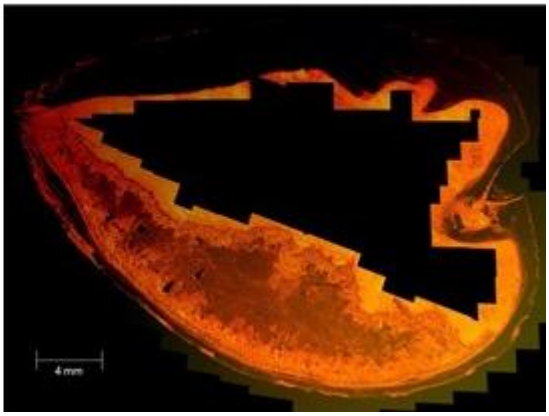

CM #27909

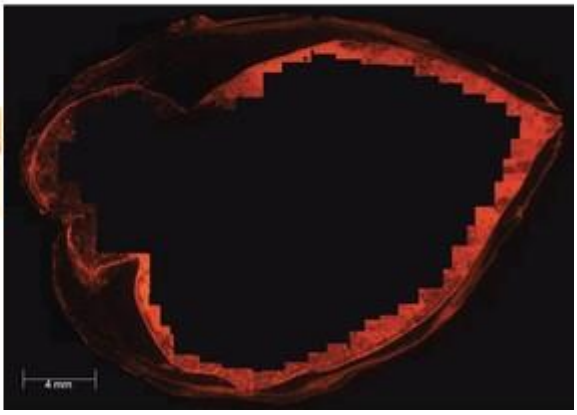

CM #27921

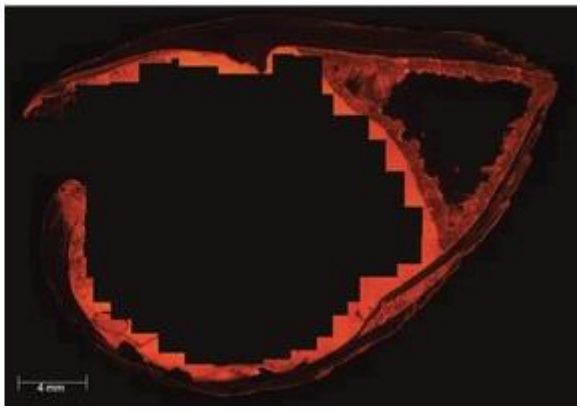

MCP-1

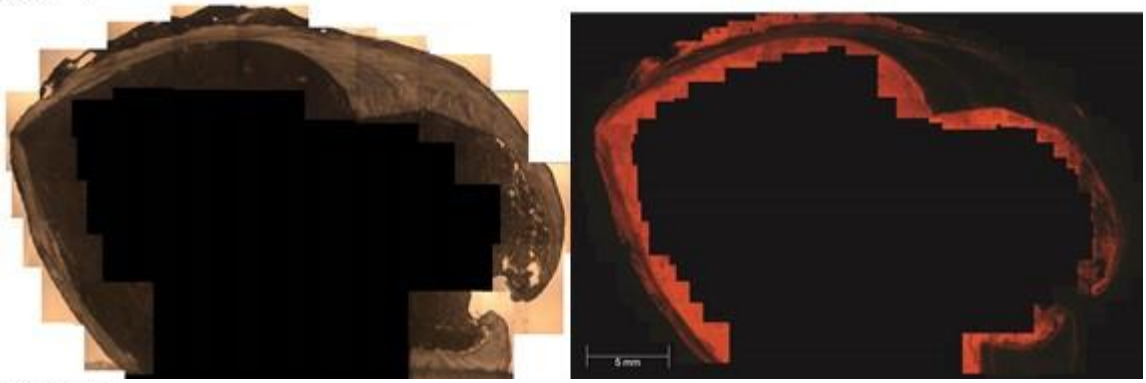

MCP-5

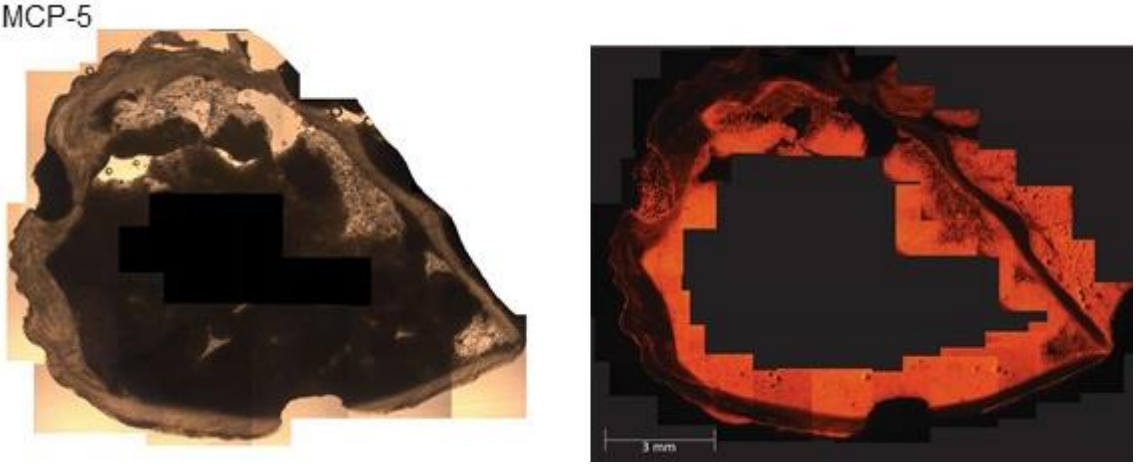

MCH-1

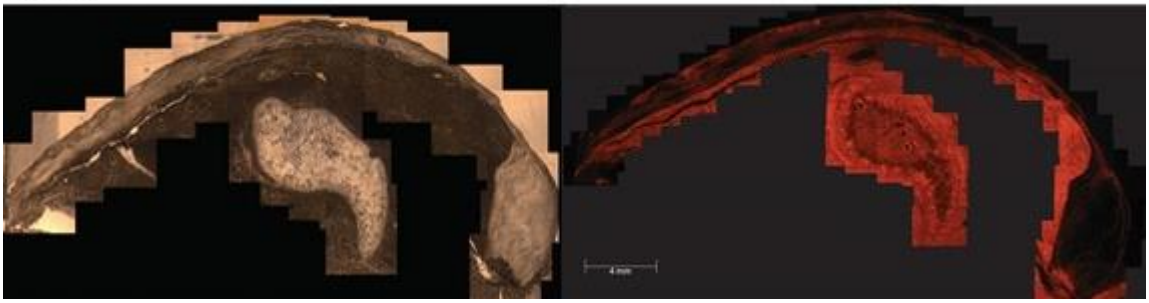

MCH-3

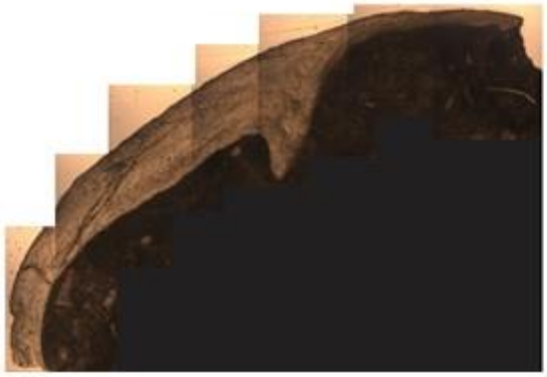

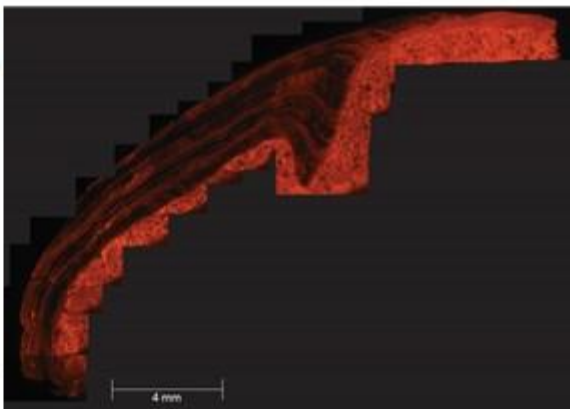

CM #68818

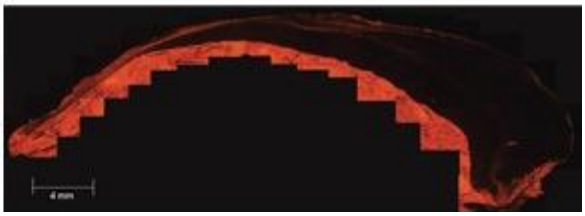

CM #68980

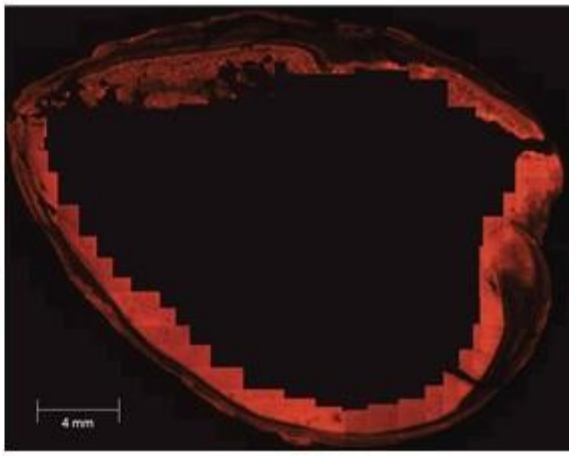

CM #68766

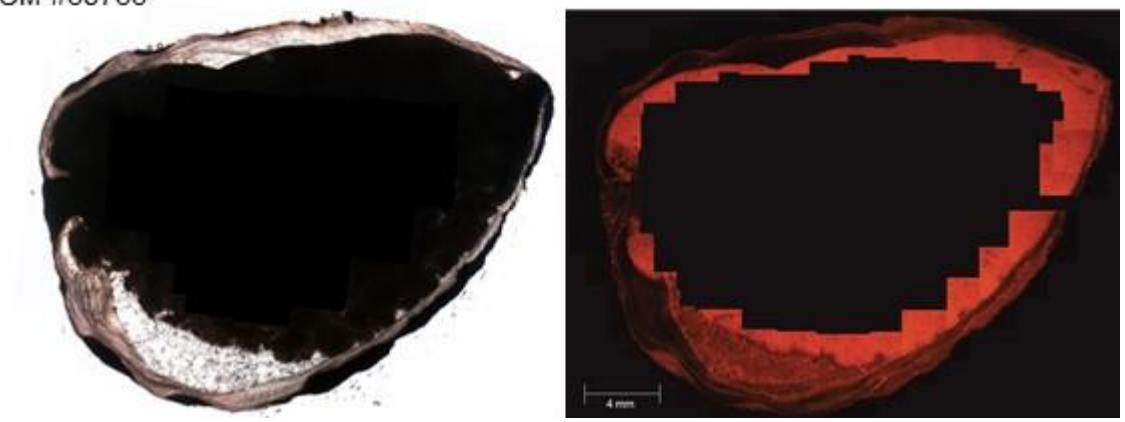

CM #78682

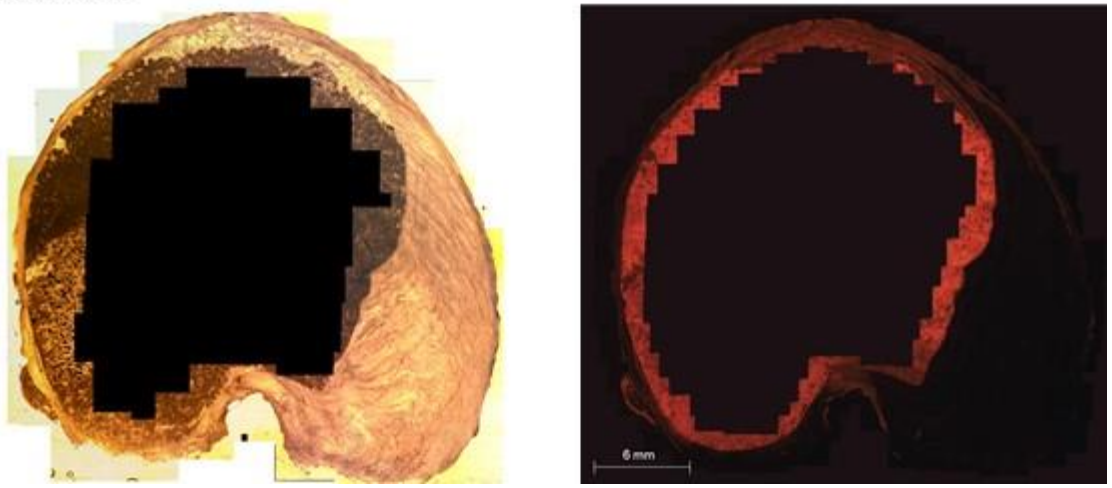

CM #78700

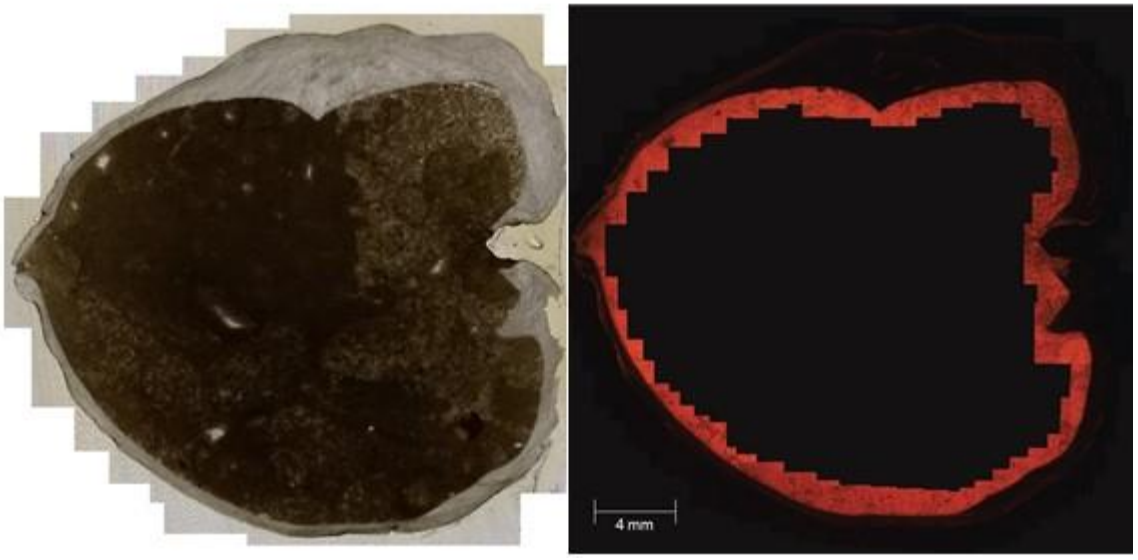

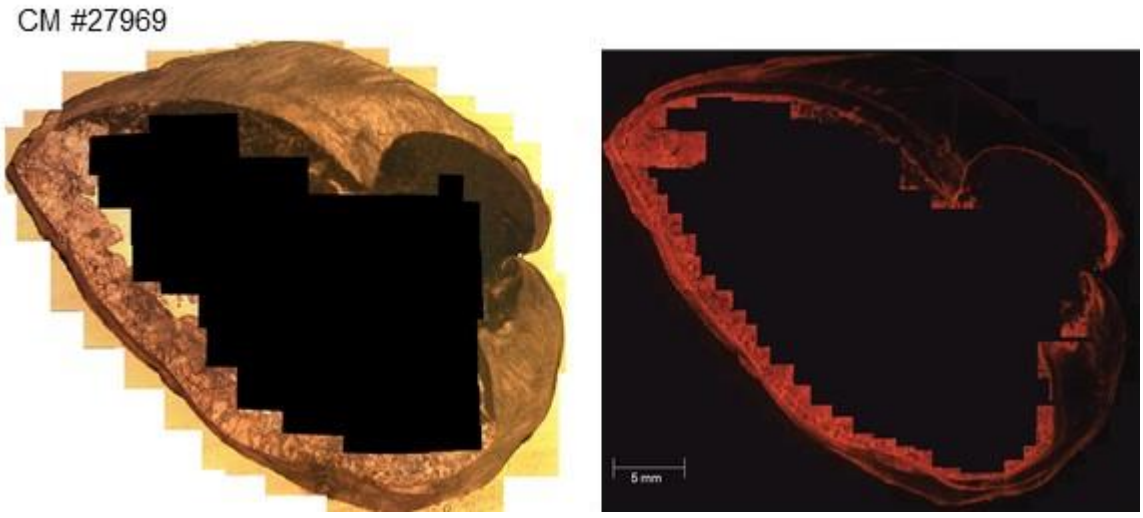

Figure 17. Plane-polarized light (right) and cathodoluminescence (left) images of Late Ordovician brachiopod shells and internal calcitic cements from the Cincinnati Arch of North America.